



**HAL**  
open science

## Exploring the dependence of chemical traits on metallicity. Chemical trends for red giant stars with asteroseismic ages

S. Vitali, D. Slumstrup, P. Jofré, L. Casamiquela, H. Korhonen, S. Blanco-Cuaresma, M. L. Winther, V. Aguirre Børsen-Koch

### ► To cite this version:

S. Vitali, D. Slumstrup, P. Jofré, L. Casamiquela, H. Korhonen, et al.. Exploring the dependence of chemical traits on metallicity. Chemical trends for red giant stars with asteroseismic ages. *Astronomy & Astrophysics - A&A*, 2024, 687, 10.1051/0004-6361/202349049 . insu-04821663

**HAL Id: insu-04821663**

**<https://insu.hal.science/insu-04821663v1>**

Submitted on 6 Dec 2024

**HAL** is a multi-disciplinary open access archive for the deposit and dissemination of scientific research documents, whether they are published or not. The documents may come from teaching and research institutions in France or abroad, or from public or private research centers.



L'archive ouverte pluridisciplinaire **HAL**, est destinée au dépôt et à la diffusion de documents scientifiques de niveau recherche, publiés ou non, émanant des établissements d'enseignement et de recherche français ou étrangers, des laboratoires publics ou privés.



Distributed under a Creative Commons Attribution 4.0 International License

# Exploring the dependence of chemical traits on metallicity

## Chemical trends for red giant stars with asteroseismic ages<sup>★,★★</sup>

S. Vitali<sup>1,2,3</sup> , D. Slumstrup<sup>2,1</sup>, P. Jofré<sup>1,3</sup>, L. Casamiquela<sup>4</sup>, H. Korhonen<sup>5,2</sup> , S. Blanco-Cuaresma<sup>6,7</sup>,  
M. L. Winther<sup>8</sup>, and V. Aguirre Børsen-Koch<sup>9</sup>

<sup>1</sup> Instituto de Estudios Astrofísicos, Facultad de Ingeniería y Ciencias, Universidad Diego Portales, Av. Ejército Libertador 441, Santiago, Chile

e-mail: [sara.vitali@mail.udp.cl](mailto:sara.vitali@mail.udp.cl)

<sup>2</sup> European Southern Observatory, Alonso de Cordova 3107, Vitacura, Chile

<sup>3</sup> Millennium Nucleus ERIS, Chile

<sup>4</sup> GEPI, Observatoire de Paris, PSL Research University, CNRS, Sorbonne Paris Cité, 5 place Jules Janssen, 92190 Meudon, France

<sup>5</sup> Max-Planck-Institut für Astronomie, Königstuhl 17, 69117 Heidelberg, Germany

<sup>6</sup> Harvard-Smithsonian Center for Astrophysics, 60 Garden Street, Cambridge, MA 02138, USA

<sup>7</sup> Laboratoire de Recherche en Neuroimagerie, University Hospital (CHUV) and University of Lausanne (UNIL), Lausanne, Switzerland

<sup>8</sup> Stellar Astrophysics Centre, Department of Physics and Astronomy, Aarhus University, Ny Munkegade 120, 8000 Aarhus C, Denmark

<sup>9</sup> DARK, Niels Bohr Institute, University of Copenhagen, Jagtvej 128, 2200 Copenhagen, Denmark

Received 21 December 2023 / Accepted 28 March 2024

### ABSTRACT

**Context.** Given the massive spectroscopic surveys and the *Gaia* mission, the Milky Way has turned into a unique laboratory to be explored using abundance ratios that show a strong dependence on time. Within this framework, the data provided through asteroseismology serve as a valuable complement. Even so, it has been demonstrated that chemical traits cannot be used as universal relations across the Galaxy.

**Aims.** To complete this picture, it is important to investigate the dependence on metallicity of the chemical ratios employed for inferring stellar ages. We aim to explore different combinations of neutron-capture, odd-Z, and  $\alpha$  elements as a function of age, particularly focusing on their metallicity dependence for a sample of 74 giant field stars.

**Methods.** Using UVES observations, we derived atmospheric parameters and high-precision line-by-line chemical abundances ( $<0.04$  dex) for the entire set of spectra, which covers a wide spread in ages (up to 14 Gyr) and metallicities ( $-0.7 < [\text{Fe}/\text{H}] < +0.1$ ). Stellar ages are inferred from asteroseismic information.

**Results.** By fitting chemical-age trends for three different metallicity groups, we estimated their dependence on metallicity. Simultaneously, we identified those exhibiting stronger correlations with time. We found that the stronger chemical-age relations ( $[\text{Zr}/\alpha]$ ) are not necessarily the ratios with the smaller dependence on metallicity ( $[\text{Ce}/\alpha]$  and  $[\text{Ce}/\text{Eu}]$ ).

**Conclusions.** We confirm the  $[\text{n-capture}/\alpha]$ -age trends for evolved stars, wherein the most significant correlation is evident in stars with solar metallicity, gradually diminishing in stars with lower iron content. The lack of homogeneity within the metallicity range highlights the intricate nature of our Galaxy's star formation history and yield production. The dependence on metallicity of the yields involving *s*-process elements and the influence of radial stellar migration pose challenges to relying solely on chemical abundances for dating stars. These findings contest the feasibility of establishing universally applicable chemical clocks that are valid across the entire Galaxy and across various metallicity ranges.

**Key words.** techniques: spectroscopic – stars: abundances – Galaxy: abundances – Galaxy: disk

## 1. Introduction

With the massive collection of data by the *Gaia* satellite ([Gaia Collaboration 2016, 2023](#)) and the ground-based spectroscopic surveys, such as APOGEE ([Majewski et al. 2017](#)), GALAH ([De Silva et al. 2015](#)), LAMOST ([Deng et al. 2012](#)), and *Gaia*-ESO ([Gilmore et al. 2012](#)), Galactic astronomy has been significantly propelled forward. The extent of these

datasets has let us build multidimensional maps of the Milky Way that have been used to decipher the timeline of events that shaped its history and evolution. In this framework, the chemical abundances of stars are powerful repositories of the composition of the birth cloud from which they originate (see, e.g., [Freeman & Bland-Hawthorn 2002](#); [Matteucci 2012](#)). The elements studied through stellar spectra carry information of the nuclear reactions and astrophysical processes that have modified the evolution of the birth cloud's chemical composition ([Freeman & Bland-Hawthorn 2002](#); [Hogg et al. 2016](#); [Jofré et al. 2017](#); [Ratcliffe et al. 2020](#)), and thus are used to reveal the chemical enrichment history of the hosting environment ([Bovy et al. 2012](#); [Minchev et al. 2017](#); [Bland-Hawthorn et al. 2019](#); [Buder et al. 2021](#)).

\* Tables with the atmospheric parameters, the line selection, and the mean abundance ratios are available at the CDS via anonymous ftp to [cdsarc.cds.unistra.fr](https://cdsarc.cds.unistra.fr) (130.79.128.5) or via <https://cdsarc.cds.unistra.fr/viz-bin/cat/J/A+A/687/A164>

\*\* Analysis of data taken as part of ESO program ID 108.22DX.

Among the multiple chemical abundance ratios, it has been found that some specific combinations are particularly informative as they show strong correlations with age (e.g., da Silva et al. 2012; Nissen 2015; Spina et al. 2018; Nissen et al. 2020). These chemical tracers, also known as chemical clocks (Nissen 2015; Tucci Maia et al. 2016), have been proposed as an alternative to determine stellar ages.

Dating stars is of paramount importance as it provides crucial insights into the timeline of several evolutionary processes, but it is very difficult to do even using one of the various existing techniques (Noels & Bragaglia 2015). Consequently, the prospects of estimated ages inferred from element abundances have been widely explored, especially for single field stars for which the age determination is even more difficult than for stars in groups or clusters (Hayden et al. 2022; Leung et al. 2023; Anders et al. 2023).

Despite the use of these valuable chemical-age relations, there are different factors that can alter these tracers, threatening their reliability and universality as age calibrators (Feltzing et al. 2017; Casali et al. 2020). A dependence on metallicity has been found by Feltzing et al. (2017), Delgado Mena et al. (2019), and Casali et al. (2020). Furthermore, although the relations might not be affected by the stellar type (Slumstrup et al. 2017), they could be affected by the techniques used for age determination (Berger et al. 2022). The lack of homogeneity in these chemical clocks can be attributed to the diverse nucleosynthetic processes that take place during a star's lifetime and to the intricate nature of chemical enrichment and star formation histories (SFHs) that undergo significant changes when we examine a considerable spatial volume (Chiappini et al. 1997; Feuillet et al. 2018; Magrini et al. 2021; Casamiquela et al. 2021).

Another important aspect to be taken into account is that stars move away from their birth places (see, e.g., Sellwood & Binney 2002; Minchev & Famaey 2010; Frankel et al. 2020). Radial gradients and chemical signatures can be significantly weakened by this stellar migration, making it difficult to reproduce the expected chemical trends. This dependence on galactocentric position and the impossibility of establishing unique chemical-age trends across the Galaxy correlates with the radial fluctuations in SFH, which in itself also creates a dependence of the stellar yields on the metallicity of the considered environment (Magrini et al. 2009; Casamiquela et al. 2021; Viscasillas Vázquez et al. 2022; Ratcliffe et al. 2023, 2024).

All these effects needed to be considered to establish reliable chemical-age calibrations. To this end, it is indispensable to have high-precision abundances to minimize the effects of internal abundance determination errors and to disentangle the different processes that might play a role in altering the relations. In addition, accurate ages determined from a separate reliable method are needed for a solid study of this kind.

Slumstrup et al. (2017) confirmed the tight correlation between  $[Y/Mg]$  and age discussed by Nissen (2015) for six evolved stars at solar metallicity in four open clusters, extending the validity of the  $[Y/Mg]$  chemical clock from dwarfs to red giants. A later study of the red giant  $\epsilon$  Tau in the Hyades at super-solar metallicity was found to fall just above the solar twin relation (Arentoft et al. 2019). This suggests that the chemical clock for evolved stars could also depend on  $[Fe/H]$  as solar analog stars (Feltzing et al. 2017). More recently, Berger et al. (2022) demonstrated that the  $[Y/Mg]$ -age relation behaves differently for stars other than solar twins. This evidence may indicate that the picture of chemical tagging is more complicated for giants than otherwise expected; that is, poorly understood mixing pro-

cesses happening in their atmospheres might have an impact on their abundances.

At the moment GALAH is the only large-scale spectroscopic survey that provides yttrium (Y) abundances, but this is focused on main-sequence and subgiant stars. Hayden et al. (2022) used GALAH data for main-sequence turn-off stars to show that a precision of  $\sim 0.05$  dex was not sufficient to calibrate different chemical clocks, even if ages were estimated with a precision of 1–2 Gyr. It is noteworthy that in a recent study, Walsen et al. (2024) improved both abundance measurements and star selection.

Asteroseismology is currently one of the most precise ways to determine ages for single field stars (Chaplin & Miglio 2013; Chaplin et al. 2014), especially for red giant (RG) stars (Miglio 2012; Anders et al. 2023), which are bright enough for inferring reliable age information. In synergy with the large-scale spectroscopic surveys, asteroseismology has widely contributed to spectroscopic age determination (Pinsonneault et al. 2014). While asteroseismic ages for an abundance of stars have been made available by CoRoT (Valentini et al. 2016; Anders et al. 2017), *Kepler* (Gilliland et al. 2010; Pinsonneault et al. 2014), and K2 (Howell et al. 2014; Rendle et al. 2019), they have only surveyed parts of the sky. With the launch of the TESS mission (Sharma et al. 2018; Silva Aguirre et al. 2020), a larger part of the sky has been surveyed, thus allowing for asteroseismic ages to be used in wider studies.

In this work we use a sample of high-resolution UVES spectra of RG field stars with asteroseismic ages to explore the homogeneity and dependences of chemical clocks across metallicity. With our homogeneous high-resolution and high signal-to-noise spectra, we determine abundances and ages for more than 70 giant stars. Our analysis serves to deepen the understanding and usage of chemical clocks in the case of more evolved stars.

The paper is structured as follow. In Sect. 2 we introduce the observational data used for this work, and in Sect. 3 we explain the methods we used for abundance and age determination. In Sect. 4 we present our results for the relations between ages and chemical abundance ratios. A discussion about their implications with a conclusion can be found in Sect. 5.

## 2. Data

### 2.1. Target selection

We analyzed a sample of 74 giant stars in five K2 fields, from which we extracted their Epic identification number, their corresponding *Gaia* DR3 ID, coordinates, magnitudes, and seismic information, summarized in Tables A.1 and A.2. These stars were selected from the K2 targets already observed by APOGEE DR17 (Abdurro'uf et al. 2022), from which an assessment of the metallicity and temperature was available. This allowed us to infer the stellar ages with an error of  $\leq 30\%$  (average  $\sim 20\%$ , see Sect. 3.2 for a more detailed discussion). The inferred ages are shown for all targets at the top of Fig. 1, and shows a significant range in both age and metallicity, which serves for the purpose of this study. Thanks to the *Gaia* third data release (DR3) (Gaia Collaboration 2023) the selection focuses on mostly bright disk giants located in the solar region ( $29$  stars with  $8.5 < R_{\text{GAL}} < 9$  kpc), and the majority in the outer disk ( $9 < R_{\text{GAL}} < 10$  kpc).

At the bottom of Fig. 1 we show the Galactic positions of our targets, colored by their magnitude. In the left panel we plot the Cartesian coordinates  $X$  and  $Y$ , and in the right panel we plot the polar coordinates  $R$  and  $z$ . We can see how the stars are located

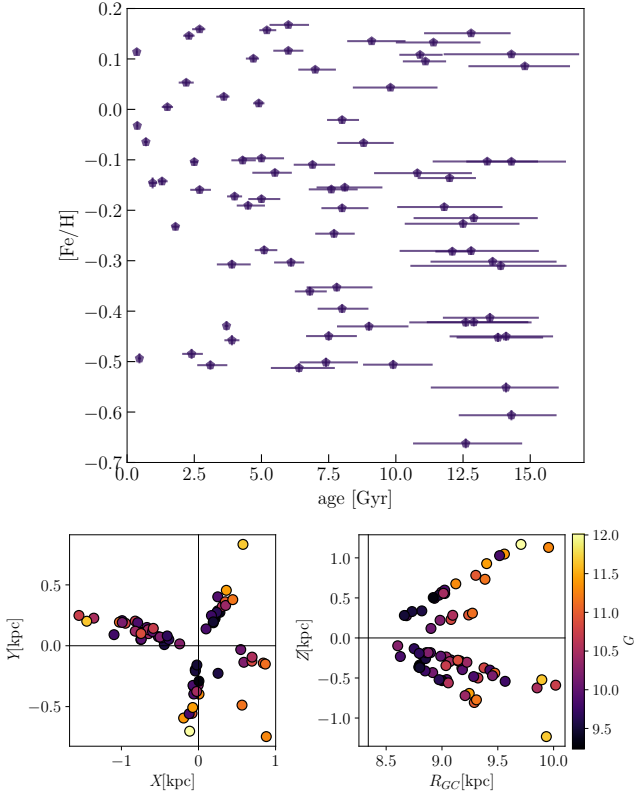


**Fig. 1.** Metallicity-age distribution and galactic positions of the observed stars. Top:  $[\text{Fe}/\text{H}]$  vs. age distribution for the proposed sample. The iron values are from APOGEE with the ages determined in this work. Bottom: Cartesian Galactic coordinates  $X$ ,  $Y$  of the targets. On the right, Galactic  $Z$  and galactocentric radii  $R_{\text{GAL}}$ . The color-coding represents the  $G$  magnitude of the sample derived from *Gaia* DR3. The black lines indicate the position of the Sun ( $X_{\odot}$ ;  $Y_{\odot}$ ;  $Z_{\odot}$ ) = (0; 0; 0) and  $R_{\text{GAL}} = 8.34$  placed at kiloparsec scale.

at different positions, and that toward the outer disk, the stars are about 1 kpc above (or below) the Galactic plane.

## 2.2. Spectral observations and data reduction

We followed up the selected APOGEE DR17 targets with UVES, a cross-dispersed echelle spectrograph mounted on the Very Large Telescope (VLT), at Paranal Observatory. The data were observed under the ESO program ID 108.22DX. The spectra were taken between September 2021 and January 2022, and the configuration employed ensures a resolving power of  $R \sim 110\,000$  covering a wavelength range from 480 to 680 nm. The high quality of the spectra translates to a signal-to-noise ratio (S/N) of  $\sim 80$ – $100$  estimated by the ESO pipeline, which is also listed in Tables A.1 and A.2.

## 3. Method: Stellar analysis

We adopted the automatic pipeline presented in the work of Casamiquela et al. (2020), which relies on the public software *iSpec* (Blanco-Cuaresma et al. 2014a; Blanco-Cuaresma 2019). The workflow was personalized for our purpose to perform the correction for the barycentric velocity and the stellar radial velocity (RV). The RVs were determined using a synthetic template. The sky subtraction and the cleaning from telluric features were applied using an internal telluric line list provided

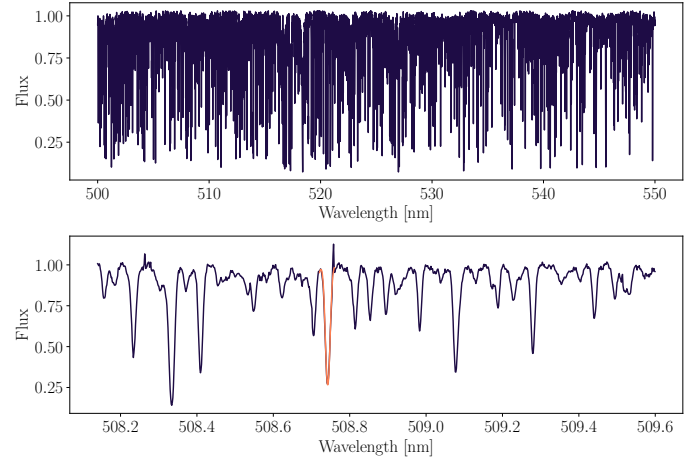


**Fig. 2.** UVES spectrum of J04034842+1551272 from  $\approx 500$  to 550 nm. The bottom panel is a zoomed-in image around the YII line at 508.74 nm. The S/N is approximately 90.

by *iSpec*. Finally, we normalized the spectra in segments using cubic splines and finding the continuum level with a median-maximum filter. An example of a portion of a normalized and velocity-corrected spectrum is shown in Fig. 2.

### 3.1. Atmospheric parameters

The atmospheric parameters ( $T_{\text{eff}}$ ,  $[\text{M}/\text{H}]$ ,  $[\alpha/\text{M}]$ , and the broadening parameters) were calculated via synthetic spectral fitting. This technique produces synthetic spectra on the fly and compares them with the observed spectrum, taking into account the uncertainties on its flux. The parameters are found by  $\chi^2$  minimization between the flux and the synthesis. We chose Turbospectrum as the radiative transfer code (Alvarez & Plez 1998; Plez 2012), which considers local thermodynamic equilibrium and the one-dimensional spherical MARCS model atmospheres (Gustafsson et al. 2008). The atomic parameters are contained in the latest version (v.6) of the line list of the *Gaia*-ESO Survey (Heiter et al. 2021), and the line selection to perform the fitting is taken from Blanco-Cuaresma (2019). Lines affected by telluric features, blends, or continuum displacement are automatically discarded. It leads to a total of 202 lines for 21 elements.

Following Blanco-Cuaresma (2019) and Casamiquela et al. (2020), we initially performed the synthesis fitting leaving effective temperature  $T_{\text{eff}}$ , surface gravity  $\log g$ , metallicity  $[\text{M}/\text{H}]$ , alpha-enhancement  $[\alpha/\text{M}]$ , and the microturbulence velocity  $v_{\text{mic}}$  as free parameters. The resolution was fitted for each spectrum to account for the broadening effects, which encompass both the rotational velocity ( $v_{\text{sin}i}$ ) and the macroturbulence ( $v_{\text{mac}}$ ) of the star. Moreover, disentangling the degeneracy between these two broadening parameters can pose significant challenges (Blanco-Cuaresma et al. 2014b). Given that our aim is not to separate all these effects individually, it suffices to optimize our spectral analysis with a single parameter. Hence, we decided to fix the  $v_{\text{sin}i}$  to  $1.6 \text{ km s}^{-1}$ , a reasonable value for giant stars. Finally, the  $v_{\text{mac}}$  was estimated using an empirical relation from the *Gaia*-ESO survey. By visual inspection we checked the goodness of the fits. We removed the spectrum with low S/N ( $\sim 30$ ) of the star EPIC 201456500, due to unsatisfactory results obtained from the fit compared to the rest of the 73 targets, with  $S/N \sim 70$ – $100$ .



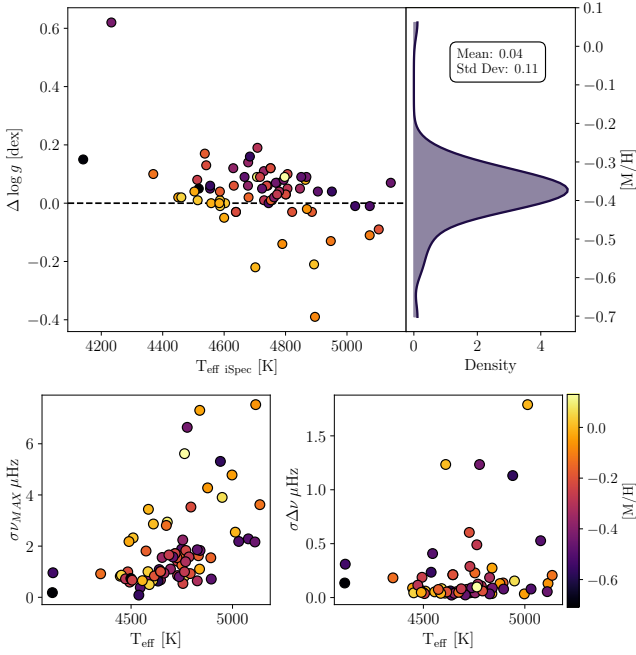


**Fig. 3.** Spectroscopic and asteroseismic surface gravity values and the asteroseismic maximum frequency and frequency separation. Top: Difference between the outcomes derived from the asteroseismic scaling relation of Eq. (1) and the spectroscopic  $\log g$ . On the right the corresponding KDE distribution is shown. Larger deviations between the two methods are observed for higher metallicity and the three coldest stars. Bottom: Uncertainties in the seismic maximum frequency and the separation  $\Delta\nu$  are depicted as a function of temperature. In all cases, the color-coding is determined based on the global metallicity calculated using iSpec.

All targets have seismic measurements, thus making it possible to validate our results with those obtained considering the seismic information. To do so, for a second run of spectral fitting, we adopted the scaling relation from asteroseismology (Brown et al. 1991; Kjeldsen & Bedding 1995) that involves the frequency of maximum power  $\nu_{\max}$  from the K2 catalog to infer  $\log g$  as

$$\log g = \log \left( \left( \frac{\nu_{\max}}{\nu_{\max\odot}} \right) \cdot \left( \frac{T_{\text{eff}}}{T_{\text{eff}\odot}} \right)^{1/2} \right) + \log g_{\odot}, \quad (1)$$

where we follow Heiter et al. (2015) and adopt the solar values  $\nu_{\max\odot} = 3100 \mu\text{Hz}$ ,  $T_{\text{eff}\odot} = 5777 \text{ K}$ , and  $\log g_{\odot} = 4.44 \text{ dex}$ . To achieve this, we used the temperatures determined in the previous run. We proceeded to compute  $\log g$  values using the provided equation. This independent determination of  $\log g$  gives us a further validation of internal consistency between our parameters and the ones that can be derived from asteroseismology.

The relation in Eq. (1) is extrapolated from the Sun. Since we apply it here for giants, deviations should be expected, which have been quantified in the literature, for example with studies of binary systems, parallaxes, and comparisons to interferometry. Asteroseismic masses have been shown to be accurate to better than 8% (Stello et al. 2016; Miglio et al. 2016; Brogaard et al. 2016) and radii to better than 4% (Silva Aguirre et al. 2012; Huber et al. 2016; Sahlholdt & Silva Aguirre 2018). Assuming a stellar mass of 1.2 solar masses and a radius of  $10 R_{\odot}$ , this translates to an accuracy on  $\log g$  better than 0.04 dex.

A comparison of the spectroscopic and asteroseismic  $\log g$  results appears in Fig. 3. The stars are sorted according to their

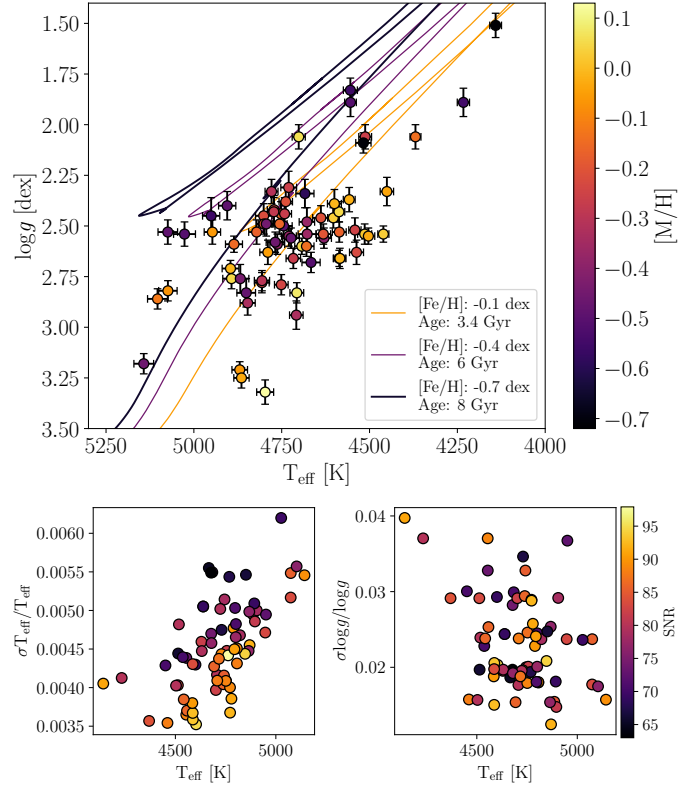


**Fig. 4.** Kiel diagram and parameter uncertainties of our sample. Top: Kiel diagram of the entire spectroscopic sample. The parameters and their errors are derived with spectral synthesis. All spectra are color-coded by their global metallicity. Three examples of BaSTI isochrones, used when fitting with BASTA, are superimposed with different colors according to their ages and  $[\text{Fe}/\text{H}]$  values. They are zoomed-in around the evolutionary stage of our targets. Bottom: Relative uncertainties on  $T_{\text{eff}}$  and  $\log g$  as a function of temperature and color-coded by the S/N of the targets.

temperature, and color-coded according to their metallicity. For most of the stars the agreement between the two determinations is within 0.2 dex, with a few exceptions that differ more. These uncertainties might stem both from increased variability in  $\sigma_{\nu_{\max}}$ , and  $\Delta\nu$  (as presented by the two lower subplots of Fig. 3) and from the larger errors on the temperatures of warmer giants (as shown at the bottom left of Fig. 4). For the two coldest outliers the  $\log g$  values computed with the seismic relation exceed the spectroscopic values by more than 0.2 dex. Despite conducting a visual inspection, no issues were identified in their fits. Consequently, we opted not to exclude these cases. However, in light of these findings, caution must be taken when interpreting the results for these three giants, given that the accuracy may be compromised for such cold stars.

After we derived the  $\log g$  using Eq. (1), we assessed again the other atmospheric parameters by fixing the asteroseismic  $\log g$ . This procedure was iterated to ensure consistent parameters, specifically until the asteroseismic  $\log g$  aligns with that utilized in the previous step to derive the spectroscopic atmospheric parameter. Our final parameters are thus those that combine both spectroscopic temperatures and metallicities with seismic  $\log g$ . These appear in the Kiel diagram in the upper panel of Fig. 4. In the same plot we illustrate, as an example, three isochrones from a Bag of Stellar Tracks and Isochrones (BaSTI, Hidalgo et al. 2018; Pietrinferni et al. 2021). We selected three age and metallicity values to represent our stars, all of which lie

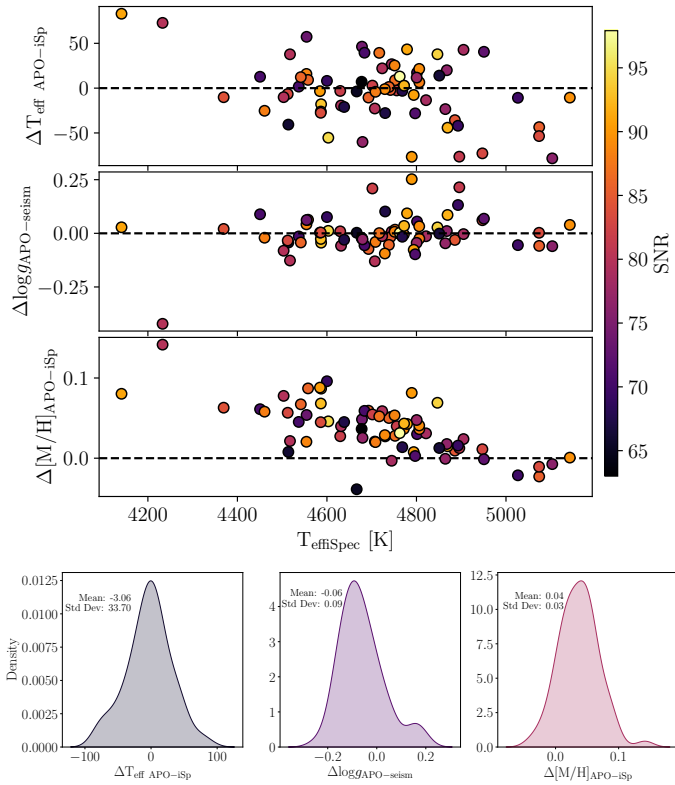


**Fig. 5.** APOGEE comparison. Top: differences between our computed and adopted atmospheric parameters and the APOGEE results as a function of spectroscopic  $T_{\text{eff}}$ . The color-coding expresses the S/N of the targets. The temperatures and metallicities were directly derived from spectroscopy, while the  $\log g$  were calculated using the scaling relation of Eq. (1). Bottom: Kernel density estimation of the three deltas together with their mean differences and dispersions.

within the giant evolutionary stage. A more comprehensive discussion about the age derivation procedure follows in Sect. 3.2.

It is possible to see the extension of the metallicity range covered by the sample:  $-0.7 \lesssim [\text{M}/\text{H}] \lesssim +0.1$ . The two coolest stars are the most metal-poor ones. iSpec estimates the uncertainties for the atmospheric parameters from the covariance matrix (the square root of the diagonal elements) computed by the least squares algorithm, and they are plotted at the bottom of Fig. 4. For the temperature the average uncertainty is 21 K and the relative uncertainties increase for hotter temperatures and for lower S/N. The seismic  $\log g$ , however, remains unaffected by such trends, even with a temperature change of 21 K, resulting in a variation of approximately 0.001 dex. For the spectroscopic  $\log g$  the average value of the relative uncertainty is  $\sim 0.02$  with a spread around 0.01, but no evident trend is present in the right panel at the bottom of Fig. 4.

Since the stars were targeted as a follow up from APOGEE observations, it is natural to compare our results with those obtained from APOGEE DR17. A comparison for temperature, surface gravity and metallicity is illustrated in Fig. 5. The differences (APOGEE-ours) are plotted in three different panels starting from the spectroscopic temperature at the top, the seismic gravity in the middle, and the metallicity at the bottom.

In addition, in the same plot we show the distribution of the differences of all three parameters, with the corresponding mean and standard deviation indicated in each panel. It is possible to see that the parameters are generally consistent for the two methods exhibiting larger deviations in the cases of the

most metal-poor and most metal-rich and hotter stars. Given that these parameters are correlated, the scatter for the hotter giants can be attributed to the increase of the errors with the temperature. However, for the temperatures and  $\log g$  the mean differences reported in the histograms are within the average parameter uncertainties. For the global metallicity  $[\text{M}/\text{H}]$  there is an offset of around 0.05 dex, which exceeds the average combined uncertainties  $\bar{\sigma}_{[\text{M}/\text{H}]} \sim 0.02$  dex. This variation is higher for colder temperature and it decreases for  $T_{\text{eff}}$  higher than  $\sim 4800$  K. This offset, together with the scatters found, can be explained by the differences in methodologies, analyses, and calibrations (see, e.g., Jofré et al. 2019; Jönsson et al. 2020; Hegedűs et al. 2023, for extensive discussions).

### 3.2. Age determination

All stars in this study are in the giant phase of their evolution. Therefore, we expect them to be low- and intermediate-mass stars undergoing H-shell burning. Since they are typically bright, this category is a perfect benchmark for studying the ages of field stars located at different distances from the Sun using asteroseismology. To this end, we used the public BAYesian STellar Algorithm (BASTA, Silva Aguirre et al. 2015; Aguirre Børsen-Koch et al. 2022). It is a Python-based code that infers stellar properties by matching observations to grids of stellar models. In our case, we employed the updated isochrones from BaSTI.

As observables, we used the  $T_{\text{eff}}$  and  $[\text{Fe}/\text{H}]$  derived by our spectral analysis, and the large frequency separation  $\Delta\nu$  and frequency of maximum power  $\nu_{\text{max}}$  from the K2 catalog listed in Tables A.1 and A.2. The model values employed for fitting the frequency separation were calculated based on the corrected scaling relation by Serenelli et al. (2017). Additionally, we used the magnitudes  $J$ ,  $H$ , and  $K$  from 2MASS (Cutri et al. 2003) with the Bayestar reddening map (Green et al. 2019) and the extinction coefficients from Table 6 in Schlafly & Finkbeiner (2011). The corrected magnitudes together with the parallaxes from Gaia DR3 were then used to match to the synthetic magnitudes of the stellar models. With this information we determined ages, final masses, and  $\log g$  for the entire sample.

We matched the observations to the set of BaSTI isochrones computed with core overshooting, atomic diffusion, and mass loss enabled (case 4 in Table 1 of Aguirre Børsen-Koch et al. 2022) deemed appropriate for this sample following Stokholm et al. (2023). Our results of ages can be checked for consistency by comparing the best BASTA parameters with the spectroscopic values, which are plotted in Fig. 6. We can see good agreement; there is a mean difference of 46 K with a dispersion of 40 K for the temperature and a 0.02 average difference with 0.09 in dispersion for  $\log g$ .

### 3.3. Chemical abundances

We measured the chemical abundances for the following families of elements:  $\alpha$ -capture (Mg, Si, Ca, Ti); odd-Z (Na, Al, Sc, Cu, V); iron-peak (Cr, Mn, Fe, Co, Ni, Zn); neutron-capture (slow-processed: Sr, Y, Zr, La, Ce, Nd; rapid-process: Eu). We fixed the atmospheric parameters calculated as explained in Sect. 3.1. We proceeded with spectral synthesis adopting the same radiative code and atmospheric model as for the stellar parameters. We determined the mean abundance ratios  $\left\langle \left[ \frac{X}{\text{Fe}} \right] \right\rangle$  using the line-by-line absolute abundances of each element. To be able to compare the chemical relations with those in the literature (see Sect. 4.3), we expressed the bracket abundances with respect

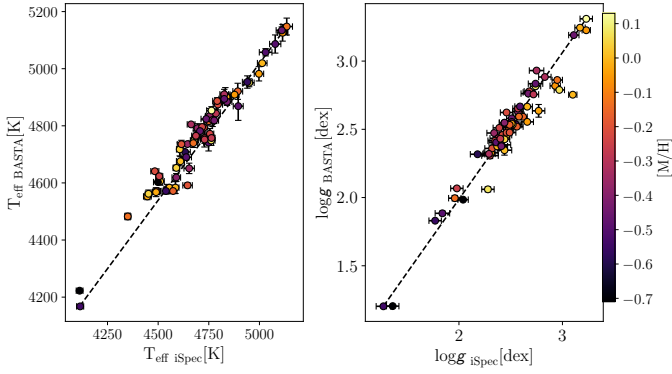


**Fig. 6.** Comparison between the properties from the spectroscopic analysis (iSpec) and stellar inference (BASTA). Left: surface temperature color-coded according to the derived spectroscopic metallicities. Right: same comparison, but for the  $\log g$  parameter.

to the Sun by adding the absolute  $\left[\frac{X}{Y}\right]_{\odot}$  ratios calculated from a solar HARPS spectrum, which we took from the library of Blanco-Cuaresma et al. (2014b). The HARPS spectrum has a similar resolution to our UVES sample ( $R \sim 110\,000$ ).

We customized the line selection according to the number of lines per element. When dealing with a substantial number of measurable lines, we discarded the lines that exhibited systematically different results. Conversely, for the elements with one or two lines (Al, Cu, Zn, Sr, Ce, Eu), we relied on the quality flags *synflag* (for the blending properties) and *gf\_flag* introduced by Heiter et al. (2021). The first flag refers to the blending properties of a line, while the second indicates the quality of the  $\log gf$  value of the line. This means that we excluded lines with potentially inaccurate  $\log gf$  measurements from our analysis.

It is worth noting that our analysis was done in local thermodynamic equilibrium (LTE). It has been demonstrated that for the solar metallicity range non-LTE (NLTE) effects have little impact on the computation of abundances (e.g., Bergemann et al. 2011; Nissen 2015; Mashonkina et al. 2019; Amarsi et al. 2020; Liu et al. 2020) with respect to more metal-poor companions. Nevertheless, recent works by Alexeeva et al. (2023) and Storm & Bergemann (2023) examined the impact on NLTE for classical elements used as chemical clocks, such as yttrium. They demonstrated that for late-type stars, the corrections concerning Y II lines do not exceed  $\approx 0.12\text{--}0.15$  dex close to solar metallicity. The deviations can be more severe for metal-poor red giants, and they exceed 0.5 dex only for  $[\text{Fe}/\text{H}] < -3.0$ , a metallicity range that falls outside of the coverage of our sample.

It is also important to consider that the number of suitable lines for abundance determination can considerably differ from one element to another. Elements with fewer lines (e.g., Mg I, Sr I, Zr II) may be more susceptible to the influence of atomic or molecular data uncertainties and blends due to the lower statistics of the measurements. All these effects systematically contribute to the overall uncertainty in the determination of abundance ratios, and separating these effects can be challenging.

We decided to compute the uncertainties of the abundance ratios by perturbing the spectra within their flux errors and by repeating the entire analysis (the synthetic spectral fitting both for the atmospheric parameters and for the abundances) ten times. By taking the mean and the standard deviation of these repeated measurements, we inferred the average dispersion of our abundance measurements as a response of the S/N of our

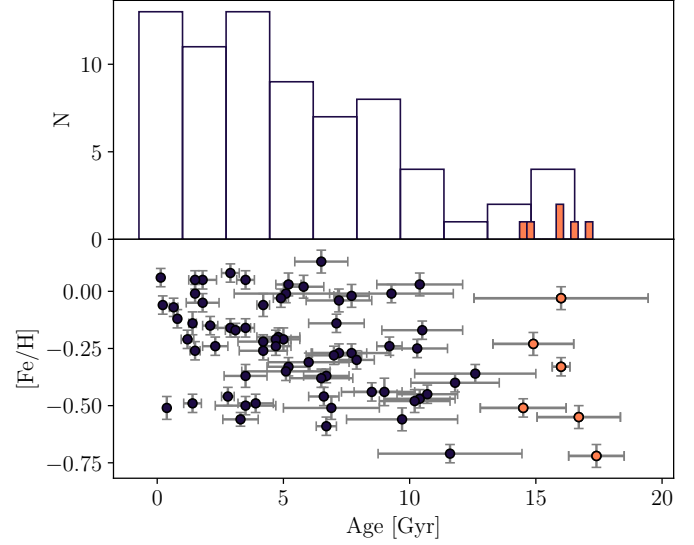


**Fig. 7.** Ages and metallicity values of our stars. Top: histogram of the age distribution of the giant sample. The stars for which we inferred ages greater than the age of the Universe, i.e.,  $>14$  Gyr are shown in orange. Bottom: age-metallicity distribution following the same color-coding.

spectra. We note that this represents an internal precision of our abundances, and not a measurement of their accuracy. For the purpose of this paper, which is to test the relations of these abundances with ages as a function of metallicity, we are more interested in the relative difference among our measurements, and thus we aim to reach high precision. For all the elements the internal precision is around 0.01–0.02 dex, with a maximum of 0.04 dex for strontium and zirconium.

Complete tables providing the atmospheric parameters, the line selection, and the mean abundance ratios with their associated uncertainties are available as online material.

## 4. Results

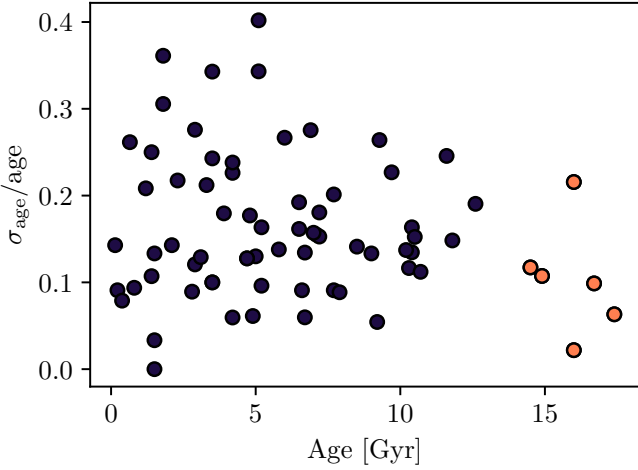
### 4.1. Age-metallicity relation

Figure 7 depicts the distribution of the resulting ages in the upper panel and the age-metallicity relation (AMR) in the lower panel. Our sample hence covers ages of the entire range of cosmic history, from very young to very old stars. The range in metallicity is also significant, allowing us to have an AMR to study the chemical evolution of the Milky Way. As in previous studies (e.g., Silva Aguirre et al. 2018; Feuillet et al. 2019), the AMR of our stars shows no correlation, though we lack young stars at low metallicity. Nevertheless, the scatter is very large, in fact much larger than the uncertainties. This underscores the complexity and dynamics of our Galaxy, implying that relying solely on this relationship is insufficient for constraining the formation and the chemical evolution of the Milky Way.

Despite the improved precision in our abundances and accuracy in our ages, with this sample we are not able to see the dual age-metallicity relation recently discussed by Nissen et al. (2020), Jofré (2021), and Sahlholdt et al. (2022). This might be due to the fact that our stars span a wide range of Galactic volumes as well as metallicities.

In Fig. 7 it is possible to see that six stars show nonphysical ages (age  $> 14$  Gyr). This group includes one of the two most metal-poor and coolest stars within the sample. For the





**Fig. 8.** Relative age uncertainties for the entire sample. Stars older than 14 Gyr are shown in orange.

entire group we checked the values of their  $\alpha$  abundances (using Mg, Ca, Si, and Ti) finding  $[\alpha/\text{Fe}] > 0.3$ . We attempted to utilize isochrones with  $\alpha$  enhancement for this subsample, but the results did not improve significantly. We thus decided to not consider these stars in the analysis, reducing the sample from 72 to 66 stars. The challenge of age calculation is evident from Fig. 8, displaying the relative uncertainties, which extend up to 40% and a mean uncertainty of  $\sim 10\%$ .

#### 4.2. Abundance-age trends

For two stars we measured very high abundances of all  $s$ -process elements, hinting toward pollution from an asymptotic giant branch (AGB) star. The abundances thus cannot be used for studying the chemical evolution of the Galaxy and were removed from our analysis. The study of their binary nature will be published in a complementary paper. This cut reduced the sample to 64 stars.

In Fig. 9 we show the abundance ratios as a function of stellar age for the stars in our sample that had reliable ages and no signs of binarity. Each panel shows a different element. We note that most metal-poor and old stars are enhanced in the  $\alpha$  elements (Mg, Si, Ca, Ti). There is a general increasing trend of  $[\alpha/\text{Fe}]$  with stellar ages. This can be seen as the result of chemical evolution, which is considerably shaped by the yields of SN type II and SN type Ia (hereafter SN II and SN Ia, respectively) occurring on different timescales (Matteucci 2016). The correlation coefficients for each  $[\text{X}/\text{Fe}]$  ratio were computed and are reported in Table 1. However, the purpose of this work is not fitting  $[\text{X}/\text{Fe}]$ -age trends, but investigating the properties of various element combinations in relation with stellar age and chemical evolution.

Our trends agree with previous chemo-chronological studies conducted on solar-like stars (Delgado Mena et al. 2019; Nissen et al. 2020; da Silva et al. 2012) where calcium exhibits a less pronounced correlation, while Na abundances lie on the opposite and spread out trend, as shown by its negative correlation coefficient. Referring to the models presented by Kobayashi et al. (2020) for sodium (Na), the trend within a comparable metallicity range to ours does not exhibit significant differences. Additionally, it is important to remember that Na abundances are heavily influenced by NLTE effects (Andrievsky et al. 2007), which we do not take into account in this study. In addition,

we are studying giants, which have likely undergone mixing processes. These factors can potentially blur our chemical-age relation. In the case of calcium (Ca) this observation may be partially attributed to the contribution of SN Ia in its production (Kobayashi et al. 2020). Silicon (Si) also displays a weak increasing trend with age, possessing together with Ca the two lower  $\rho$  values among the  $\alpha$  elements. This is in agreement with Delgado Mena et al. (2019) and Nissen et al. (2020), but conflicts with the results reported by da Silva et al. (2012), who reported no discernible trend.

Generally, the behavior of the  $\alpha$  elements is opposite to that of the  $s$ -process elements, which have a lower ratio with respect to iron for older stars, as proved by the negative  $\rho$  values for this family of elements. There is no noticeable difference between the lighter strontium (Sr) and yttrium (Y) and the heavier zirconium (Zr), lanthanum (La), and cerium (Ce)  $n$ -capture elements. As in Delgado Mena et al. (2019) and da Silva et al. (2012) the  $s$ -process element neodymium (Nd) creates a flatter and greater scatter trend with respect to the other  $s$ -process elements. This is especially true for older stars, while its production appears to have increased in more recent times. It also exhibits a less negative correlation coefficient than the other heavy elements.

For the  $r$ -process element europium (Eu) the observed scatter can be attributed to the challenges in measuring its abundances. Our measurements were limited to only one line ( $\lambda 664.5101$  nm), located in the reddest part of the spectrum. An example of the Eu line profile for J04034842+1551272 can be seen in the right panel of Fig. 10. Nonetheless, the enhancement for the oldest giants agrees with the expected increase in Eu for lower  $[\text{Fe}/\text{H}]$  values (Delgado Mena et al. 2019; Tautvaišienė et al. 2021).

Barium (Ba) is a good representative element for the  $s$ -process family and the abundance of Ba was measured for the entire sample. However, we have opted not to report our results. The two Ba II lines used in our analysis (585.366 and 614.141 nm, which are also shown in Fig. 10) require careful assessment. These lines are known to have a strong correlation with stellar activity (Reddy & Lambert 2017). Furthermore, the intensity of the lines identified in our sample of giants raised concerns about entering a regime influenced by saturation and NLTE effects (Liu et al. 2020; Baratella et al. 2021). For the star J04034842+1551272 plotted in Fig. 10, the Ba lines are saturated.

For the iron-peak elements, as in other studies, we did not find any specific correlations. Cobalt (Co) and nickel (Ni) show an increasing trend for stars younger than the Sun with the oldest experiencing a flattening trend. Chromium (Cr) and manganese (Mn) exhibit more dispersed trends, possibly indicating the influence of AGB stars in their formation processes (Kobayashi et al. 2020). The increasing trend with age shown by zinc (Zn) can be explained by the complex combination of astrophysical production sites of this element (Matteucci et al. 1993; François et al. 2004; Hirai et al. 2018). A part of being synthesized by SN Ia as other iron-peak elements, Zn can be produced by exploding supernovas (Kitaura et al. 2006; Kobayashi et al. 2006) or even more energetic sources such as hypernovae (HNe) have been proposed (e.g., Kobayashi et al. 2006). Bisterzo et al. (2005) reported an increasing trend of  $[\text{Zn}/\text{Fe}]$  in progressively metal-poor stars, possibly indicative of older stellar populations. They connected this trend with the weak  $s$ - $r$  processes mechanism, which contributes to Zn production within massive stars.

Finally, among the odd- $Z$  element, aluminum (Al) shows a strong increasing trend with age, which makes this explosive element a valuable component for chemical tagging (Jofré et al.



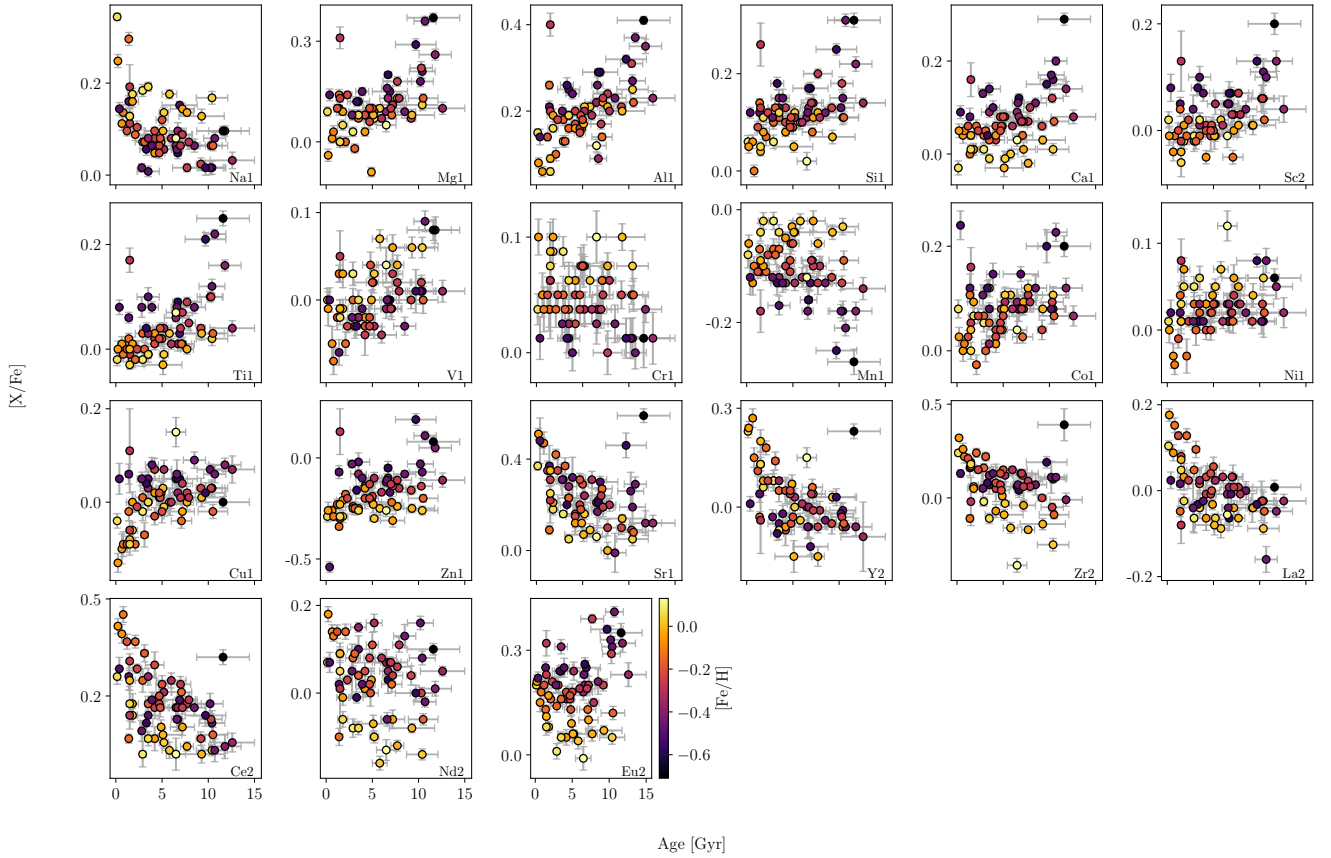


**Fig. 9.**  $[X/Fe]$  as a function of age, for stars younger than 14 Gyr. The stars are color-coded according to iron abundance, and the panels are ordered according to the atomic number of each element.

**Table 1.** Pearson correlation coefficients  $\rho$  for each  $[X/Fe]$  ratio in relation with stellar age.

Element	$\rho$	Element	$\rho$	Element	$\rho$
Na1	-0.45	V1	0.55	Sr1	-0.38
Mg1	0.53	Cr1	-0.23	Y2	-0.5
Al1	0.56	Mn1	-0.36	Zr2	-0.39
Si1	0.49	Co1	0.36	La2	-0.55
Ca1	0.43	Ni1	0.36	Ce2	-0.55
Sc2	0.48	Cu1	0.4	Nd2	-0.23
Ti1	0.52	Zn1	0.45	Eu2	0.27

which is mostly produced by CCSNe (Ou et al. 2020) with a smaller contribution from SN Ia (Kobayashi et al. 2020). Scandium (Sc) presents a moderately smaller decrease over time, but a trend is still visible, being mostly produced by CCSNe. Copper (Cu) is a more complex case; it lacks a clear trend with time, being partially formed from AGB stars, while models for Sc attributed its formation to SN Ia (Kobayashi et al. 2020).

#### 4.3. Comparison with established chemical clocks

To validate our chemical abundance measurements, we consider the well-studied chemical clocks, which relate  $[Y/Mg]$  (e.g., da Silva et al. 2012; Nissen 2015),  $[Y/Al]$  (e.g., Nissen 2016; Spina et al. 2016, 2018; Casamiquela et al. 2021), and age. In the case of Y and magnesium (Mg), these two abundances are representative of the families of the n-capture and  $\alpha$  elements. Since these two groups of elements are produced through various production channels that operate on different timescales, their dependences with time can be seen as a direct consequence of the chemical evolution within our Galaxy. Magnesium, like other  $\alpha$ -elements, primarily originates from CCSNe and it contributed to the enrichment of the interstellar medium (ISM) on earlier and shorter timescales. On the other hand, Y is an s-process element that comes from low- and intermediate-mass stars (1–8  $M_{\odot}$ ) during their AGB phase. These stars release their elemental yields over significantly longer time intervals (for extensive explanations, see, e.g., Kobayashi et al. 2006; Matteucci 2012; Karakas & Lattanzio 2014, and references therein). Therefore, the ratios of these element abundances enclose intrinsic galactic time information and can be used as age indicators.

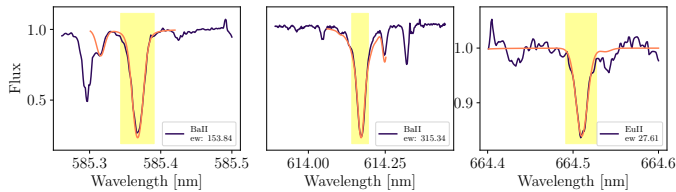


**Fig. 10.** Profile of two Ba II lines at 585.366 and 614.171 nm and the Eu II at 664.5101 nm for the giant J04034842+1551272. The darker lines represent the observed spectra, orange denotes the synthetic fit, the yellow denotes the area in which the abundances are computed. The values of the equivalent widths of each line are shown in each panel.

2020; Casamiquela et al. 2021; Hawkins et al. 2015; Das et al. 2020). A similar strong trend can be seen for vanadium (V),

**Table 2.** Definition of metallicity groups used to divide the clean sample with the respective number of stars for each group.

Group	[Fe/H] range	Number of stars	Color
Solar	[−0.1, 0.1]	18	Blue
Mix	[−0.35, −0.1]	24	Yellow
Poor	[−0.7, −0.35]	20	Red

**Notes.** These groups exclude stars eliminated due to age or chemical cuts (in addition to the two potential blue stragglers discussed in Sect. 4.3).

The primary sources of Al are CCSNe (Bisterzo et al. 2014; Fujimoto et al. 2020). As stated before, these stars act on significantly shorter timescales compared to AGBs, which are primarily responsible for the production of neutron-capture elements.

For Y and Mg we compare our results with the relations discussed by Nissen et al. (2017) and by Berger et al. (2022). These relations are based on solar twin data and were derived in LTE. Ages were calculated with isochrones in Berger et al. (2022), and via asteroseismic data in Nissen et al. (2017).

To best compare these results with our own, we considered only the stars with measured metallicities around solar ( $-0.1 < [\text{Fe}/\text{H}] < 0.1$ ). We call this group of stars solar for better reference, and represent it in blue throughout the rest of the work. Since our sample covers a wider range in [Fe/H], to study the dependence on metallicity we divided our sample into two additional bins: intermediate metallicity ( $-0.35 < [\text{Fe}/\text{H}] < -0.1$ ) and metal poor ( $[\text{Fe}/\text{H}] < -0.35$ ). We call the stars belonging to these divisions mix and poor, respectively. The stars from these groups are plotted in yellow and red, and their ranges and number of stars can be found in Table 2 together with the solar group.

The abundance–age linear relations were estimated using the RANdom SAMple Consensus algorithm (RANSAC; e.g., Fischler & Bolles 1981) for linear regression. RANSAC estimates the slope and intercept using repeated random subsampling to reduce the influence of highly uncertain measurements (or outliers) on the estimated relations. To account for the uncertainties in the data, we performed this regression multiple times using values from normal distributions for each abundance and age measurement. These distributions are centered around the reported measurements (see results in Table B.1) and have standard deviations based on their reported uncertainties. We fit 1000 regressors by sampling abundances and ages in accordance with their uncertainties. The final values of the linear regression coefficients and their uncertainties were computed by determining the mean and variance after these iterations.

In the top panel of Fig. 11 we present the linear relations we fit for the three metallicity groups. The shaded areas denote the literature fits including their respective uncertainties: gray represents the relation discovered by Nissen et al. (2017), while blue represents the relation of Berger et al. (2022). Comparing our solar results with the literature, we find an agreement with the relations found in the literature for solar metallicity stars. Our relation is also consistent with other studies that consider red giant branch stars (Slumstrup et al. 2017; Casamiquela et al. 2020).

The bottom panel of Fig. 11 shows the same metallicity groups for the [Y/Al] ratio. Here the comparison is performed with respect to the works by Nissen (2016) and Spina et al. (2018) that again analyze solar twin stars and ages from isochrone models, assuming LTE. The slope found in this work

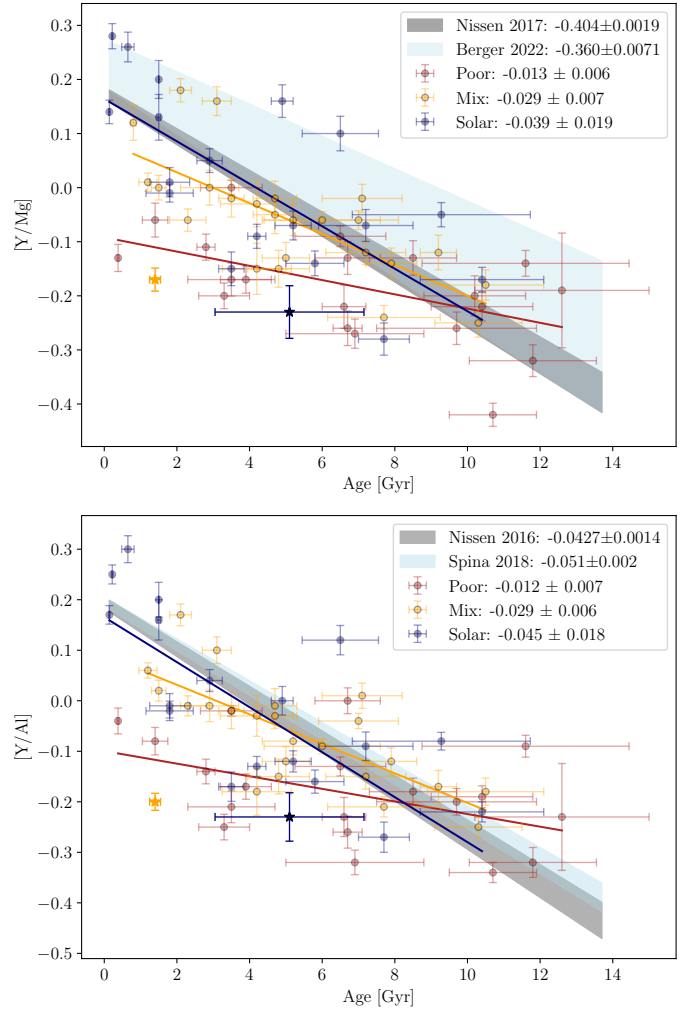


**Fig. 11.** [Y/Mg] and [Y/Al]-ages linear relations. Top: [Y/Mg] vs. ages for stars with age < 14 Gyr. Bottom: [Y/Al] vs. ages for the same stellar selection. For both panels the three solid lines represent the relation identified for the three distinct metallicity groups outlined in Table 2. The gray and light blue shaded regions display the previously established relationships from the literature derived for solar twin stars, which we compare with the findings for our solar group (in blue). The figure legends (see insets) provide the slopes of each relation along with their associated uncertainties. The two giants marked with star symbols are two possible evolved blue stragglers that have been excluded from the fitting procedures, as discussed in Sect. 4.3.

for the solar group falls within the established literature ranges. A slight deviation is noticeable for very young ages, potentially caused by the observed dispersion among younger stars. Additionally, we compared our giants with less evolved stars, specifically solar twin stars. Even so, the comparison aligns with the findings in the literature, accounting for uncertainties.

Similarly to the solar metallicity range, we performed linear regression for the mix and poor groups. The fits are plotted with a continuous line whose slope is indicated in the legend. We find for both cases that the chemical–age relation becomes flatter as metallicity decreases, which agrees with previous findings (e.g., Feltzing et al. 2017; Delgado Mena et al. 2019; Casali et al. 2020; Berger et al. 2022).

We comment on the stars J16081431–2130041 and J03573726+2425332 (blue and yellow star symbols), which have noticeably lower [Y/Mg] and [Y/Al] given their age. By

visual inspection of their spectra, we were unable to find anything particular that would lead us to conclude that the chemical abundances were incorrectly determined. The target labeled with a blue star is associated with a relatively large abundance error bar; nevertheless, this discrepancy does not account for the low abundance ratio. We further inspect the results of the ages, reaching the same conclusion that the results seem to be well behaved. We believe these stars might be evolved blue stragglers. Recent studies have shown that such stars indeed have very normal chemical abundance patterns and might not necessarily be binaries anymore (Jofré et al. 2023), but can still be explained with the merger of two stars (Izzard et al. 2018), henceforth being evolved blue stragglers. In the field, stars can have a wide range of ages; blue stragglers tend to be very hidden as they do not necessarily show oddly young ages, such as blue stragglers in clusters (Sandage 1953), blue metal-poor stars in the halo (Preston & Sneden 2000), or the stars dubbed young  $\alpha$ -rich stars (Martig et al. 2015). Chemical clocks might offer an interesting way to identify them because their chemistry predicts an older age than can be measured with standard evolutionary tracks that consider single stars.

#### 4.4. Dependence of metallicity in chemical traits

Jofré et al. (2020) discussed how many other abundance ratios that combine an  $s$ -process element with an  $\alpha$ -capture element also show a strong dependence on age. They called these abundance ratios chemical traits instead of chemical clocks, arguing that a clock has a universal dependence on time, which might not be the case for these abundance ratios. That work focused on a solar twin sample, and thus it remains to be explored if they all had a similar dependence on metallicity than the more studied [Y/Mg] discussed in the previous sections (see also Feltzing et al. 2017 and Nissen et al. 2020, for discussion). Delgado Mena et al. (2017) explored a set of FGK dwarf stars, examining various combinations of elements alongside some [s/ $\alpha$ ] ratios. Their study also revealed variability in abundance–age relationships influenced by factors such as metallicity, stellar structure, and evolution.

In this study the metallicity range is large enough to allow us to investigate the dependence of these chemical traits on metallicity. To do so, we kept the separation of the three metallicity groups listed in Table 2, and plot the abundance ratios as a function of age in Fig. 12, where we respect the color scheme of Fig. 11. Each panel shows a different trait. Each column is a different  $\alpha$ -capture element (Mg, Si, Ca, and Ti) and each row a different  $s$ -process element (Sr, Y, Zr, La, Ce, and Nd). Following the analysis discussed in the previous section, we performed linear regression fits to the data and plot with the corresponding color a continuous line in Fig. 12. From this point of the analysis we excluded the two possible blue stragglers discussed above. A table reporting the linear regression fit coefficients for the three groups can be found in Appendix B.1.

In general, we see that the chemical traits have a negative trend with age, following the same behavior as [Y/Mg], specifically that the neutron-capture element over Fe decreases with time, while the  $\alpha$ -capture element over Fe increases. We further find that the solar group (in blue) has traits with stronger correlations than the poor group (in red). The mix group lies in between. In the solar group, Zr, Sr, and then Y combined with the alphas show steeper slopes. These combinations usually show the highest correlation (as also found by Jofré et al. 2020 and Casamiquela et al. 2021), which we quantified by computing for each regression fit the Pearson correlation coefficient

( $\rho$  coefficient) reported in Table B.1. The ratios involving Ca in the denominator for Nd, Ce, La, and Y do not satisfy the criterion of having a slope greater than a threshold value set at 0.03 dex Gyr<sup>-1</sup>. This can be partially attributed to the contribution of SN Ia in the formation processes of Ca, resulting in a less pronounced correlation with age compared to the other  $\alpha$ -elements. The threshold value for the slope is adopted following the same criterion as in Jofré et al. (2020). They derived this criterion from typical observations of the slope in linear fits involving abundance ratios with Fe, which typically remain below 0.03 dex Gyr<sup>-1</sup>.

It is interesting that the [La/ $\alpha$ -elements] ratios drive the slopes to be smaller than 0.03 dex Gyr<sup>-1</sup>. However, our coefficients considering their uncertainties are comparable with the results found by Jofré et al. (2020). In this same literature work Ca does not produce considerable strong correlations with age, except when it is considered alongside Ba, an element we have opted not to include in our analysis. Neodymium displays less pronounced slopes, as expected from the scatter shown by this element in the [Fe/H]-age plane in Fig. 9.

In addition to  $s$ -process versus  $\alpha$ -capture, we studied traits that combine neutron-capture elements of  $s$ -process versus two odd- $Z$  elements: Al and V and with the  $r$ -process element Eu. Figure 9 reveals an interesting behavior for V and Al, which exhibit a strong and neat correlation with age (see Tables 1 and B.1 for specific information on each metallicity group). This characteristic makes them noteworthy candidates for chemical stellar age prediction.

Even if it is not clear what kind of sources are responsible for the production of  $r$ -process elements (e.g., neutron star mergers, magneto-rotational supernovae; for further details, see Côté et al. 2018), they constitute the main channel for  $n$ -capture nucleosynthesis before the upturn of the AGBs, after ignition of helium shell burning. Therefore, the [s/ $r$ ] ratios are promising indicators of the contribution of intermediate-mass stars compared to high-mass stars, and thus valuable tracers of chemical evolution (e.g., Magrini et al. 2018; Recio-Blanco et al. 2021).

Our results for these element are shown in the left column of Fig. 13 for the [s/ $r$ ] abundance ratio, in the middle column for the [s/V] ratio, and in the right column for the [s/Al] ratio. The rows are sorted in the same way as Fig. 12. Similarly to the  $\alpha$ -capture elements, the traits when considering aluminum have a dependence on metallicity such that the solar group yields a linear regression fit with age that has a steeper slope than the poor group, with the mix group in between. This is because Al is also produced in CCSNe, at rates that are comparable to  $\alpha$ -capture elements. Also for this case, Zr is one of the elements that shows stronger slopes, followed by Y and Sr. La and Ce, while showing slightly weaker correlations, still have ratios with Al that are related with ages with slopes greater than the threshold value. The trends observed in the other odd- $Z$  element V display a comparable pattern, albeit with slightly less pronounced slopes. This behavior can be linked to the involvement of SNIa in the production of V, in contrast to Al, which is predominantly formed from CCSNe. Again, Zr and Sr exhibit stronger correlations with steeper ratios together with La, while Ce and Nd showcase more moderate trends as for the [n-capture/ $\alpha$ ]-elements ratios.

The [s/ $r$ ] abundance ratios have different dependences on age and metallicity, meaning that the stars in the solar group do not necessarily display the stronger dependences on age. It is the mixed group for which we observe the steepest slopes when examining the relationship with age. The only exceptions are [Zr/Eu], where the solar group exhibits the steepest slope, and the ratio [Nd/Eu], which presents comparable slope values for

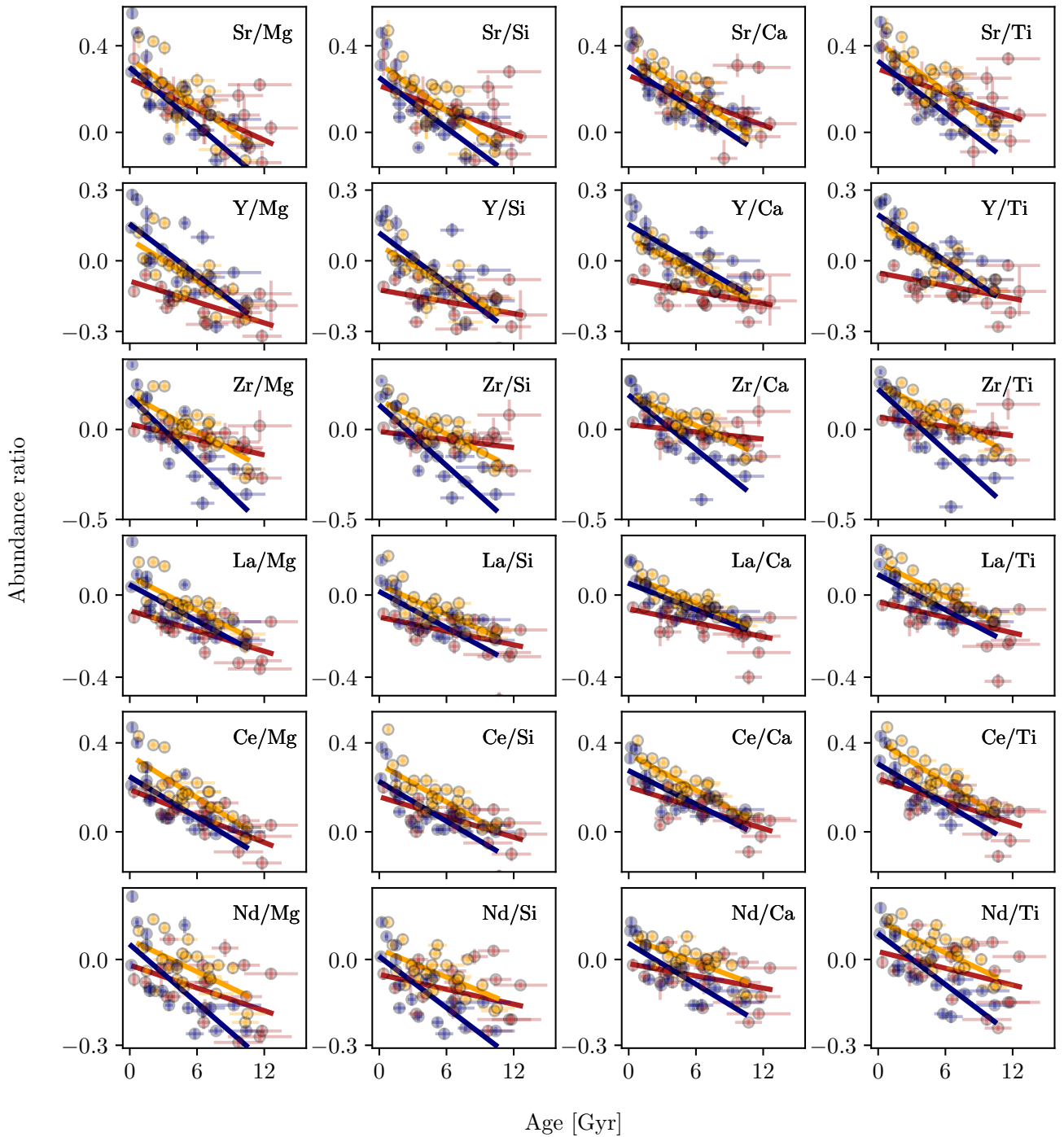


**Fig. 12.** Chemical traits as a function of age for the three metallicity groups with linear regression fits. Blue is for solar, yellow for mix, and red for poor (see Table 2). The solid lines are the linear fits to the respective metallicity groups. The stellar sample represented do not contain stars older than 14 Gyr and J16081431–2130041 and J03573726+242533.

both the mixed and solar groups. These ratios yield a correlation with age that is consistent with the *s*-process/ $\alpha$ -capture traits, namely stronger for the solar group. For the other traits, the trends are negative, but with comparable trends with age. It is important to bear in mind that the measure of Eu abundances must be approached with caution since they are based on one line (see explanation in Sect. 4.2).

Finally, the scatter of the older and more metal-poor targets that blur the age relations can be ascribed to the challenges in estimating ages, particularly for giants, resulting in

greater imprecision. This makes it more difficult to separate the pure [Fe/H] dependence from the dispersion due to the age variable.

#### 4.5. Comparing slopes

Generally, from Figs. 12 and 13 we find that all chemical traits have a similar dependence on metallicity; specifically, the strongest dependence is for solar-metallicity stars and it weakens toward more metal-poor stars. The exception is when studying



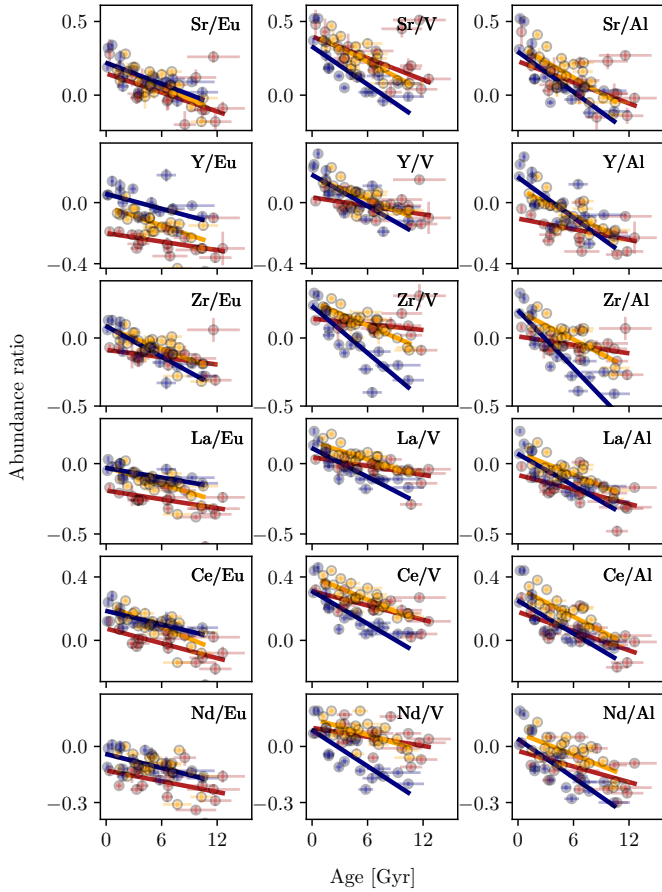


**Fig. 13.** Ratios of slow to rapid [s/r] n-capture elements, and of s-elements to vanadium and to aluminum as a function of age. The color scheme for the stars and the regression lines is the same as in Fig. 12.

only neutron capture elements and the [s/r] abundance ratio, which seems to be more independent of metallicity.

In Fig. 14 we summarize these findings by studying further the change in the slope for each trait. We plot the difference in slope of our linear regression fits for each group. The circles represent the difference in slope between the solar and the mix group, while the stars represent the difference between the solar and the poor group. The symbols are color-coded by the  $\rho$  correlation parameter of the linear regression fit found for the poor group (star symbol) and mix group (dot marker). The error bars incorporate the combined uncertainties of the differences between the ratios. The top panel of the figure summarizes the differences for the traits shown in Fig. 12 and the bottom panel summarizes the differences for the traits shown in Fig. 13.

From this figure we immediately see that Zr is the element with the strongest dependence on metallicity, followed by Y and Sr. The differences in slope for the correlations of [Zr/ $\alpha$ -capture] and [Zr/Al] are up to 0.05 dex, twice as high as any other element, while the differences for Sr and Y are lower than 0.03 dex. Similar findings are reported by Magrini et al. (2018) and Delgado Mena et al. (2017), who found a pronounced [Zr/Fe] versus [Fe/H] trend. We note however that there is a high intrinsic scatter in these relations, potentially resulting from measurements based on a single absorption line for both Zr and Al; we suggest caution in adopting these elements as possible stellar chemical-clocks. We also see that the traits that involve La and Ce have a weak dependence on metallicity; the  $\Delta$  slope values are close to zero, hence a more universal stellar chemical-clock.

The different metallicity dependence discussed above could be associated with the diverse origins and formation pathways of both light (*ls*) and heavy (*hs*) *s*-process elements, also known as first-peak elements (Sr, Y, Zr) and second-peak elements (Ba, La, Ce, Pr, and Nd), respectively. The *ls*-elements in addition to the significant contributions from the *s*-process channel (65% for Zr and 69% for Y; Travaglio et al. 2004), exhibit notable contributions from intermediate-mass AGB stars (Kobayashi et al. 2020; Goswami et al. 2024) and more massive stars (Pignatari et al. 2010). On the other hand, the primary sources responsible for these heavy *s*-process elements are the yields from low-mass AGB stars with masses of  $\leq 3 M_{\odot}$  (Lugaro et al. 2003). For both groups, the complex production chain of *s*-process elements happening in the thermally pulsing phase of AGB stars in the burning-shell regions strongly depends on metallicity (Bisterzo et al. 2014; Karakas & Lattanzio 2014; Cristallo et al. 2015; Magrini et al. 2021). This significantly challenges the uniformity of these ratios in conveying age-related information.

Another notable difference between the first and second-peak elements is the percentage of *s*-process contribution and the neutron flux within their respective sources. For the second-peak elements, both the *s*-process contribution and neutron flux are high (Travaglio et al. 2004; Karakas & Lugaro 2016). Earlier studies demonstrated that the decline in metallicity has a greater impact on elements from the first peak compared to those from the second peak. This is because the neutron flux rises as metallicity decreases, meaning that first-peak elements are expected to be more abundant at higher metallicity (Gallino et al. 2006; Cristallo et al. 2015). Consequently, it is plausible that within the range of metallicities being studied, the production mechanisms of *ls*-elements may undergo alterations.

In this context, the study of Spina et al. (2018) demonstrates that the slopes of [X/Fe]–age relationships exhibit an increase with the *s*-process contribution; that is, elements such as Zr, Y, and Sr present higher slope values (i.e., steeper), with only barium displaying even greater values. In their work the *hs*-elements, La and Ce, exhibit less steep slopes compared to the *ls*-companions (as found in our analysis) even when their *s*-process contributions are similar.

Moving to Nd, one of the heaviest elements, we observe relatively weak correlations with age. Its production pathway shows a resemblance to Ce, primarily originating from low-mass AGBs (Lugaro et al. 2003). Consequently, one might anticipate strong age correlations when Nd is examined in conjunction with  $\alpha$ -elements, similar to Ce. Referring to Bisterzo et al. (2014) the *s*-contribution of Nd is  $\approx 58\%$ , while for Ce it is  $\approx 84\%$ . These different contributions might justify the different age trends detected for the two elements.

Regarding the behavior of the  $\alpha$ -capture elements, there are not any prominent features that emerge. We can see that when Ca is considered, the difference in slope is slightly smaller. The [Y/Mg] trait has a stronger dependence on metallicity than its equivalent [Y/Ca]. As mentioned in Sect. 4.4, this may originate from the yields of SN Ia, which contribute to the release of calcium (Zenati et al. 2023).

Regarding the behavior of the *r*-process element Eu, we see that in general the dependence on metallicity is very small, and that the slopes are flatter compared to the ratios with the same n-capture elements but with  $\alpha$  or odd-Z elements in the numerators. Similar conclusions are reported in the works of Spina et al. (2018) and Delgado Mena et al. (2019). We find that most traits have negligible differences in the slope of the regression fits, except [Zr/Eu], but we have already found that Zr might be driving the metallicity dependence. The distinct behaviors of these element ratios that result in more shallow slopes can be

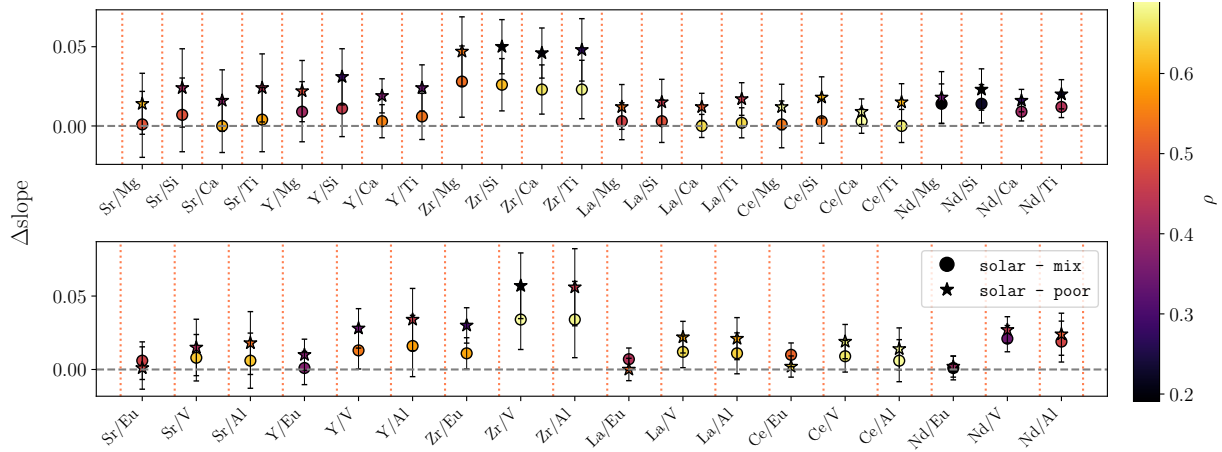


**Fig. 14.** Slope differences for each element combination of each ratio. The dot and star points specifically highlight variations between the solar and mix groups, and the solar and poor groups, respectively. The color-coding represents the correlation coefficient values. For the dot points,  $\rho$  is computed based on the mix group, whereas for the star points the correlation coefficients are derived from the poor group.

attributed to the debated origin of  $r$ -process elements. Apart from CCSNe, more exotic scenarios have been proposed as potential sources for  $r$ -process elements, including neutron star mergers (Côté et al. 2018).

The odd- $Z$  elements V and Al, when combined with neutron-capture elements, once again exhibit stronger correlations with age within the solar metallicity group. However, there is a noticeable flattening trend in the cases of Y, Zr, and La when they are combined with vanadium for the metal-poor stars. Overall, Al appears to have a lesser effect on flattening the age-metallicity relationships for lower metallicities. For both odd- $Z$  elements, their dependence on metallicity, when considering the same specific  $n$ -capture, is more significant than that of Eu and it is more similar to the  $\alpha$ -elements.

Finally, we focus on the correlation coefficient. The traits with the tighter correlation for both mix and poor are [Ce/Ca], [Ce/Al], and [Ce/Ti], which interestingly have a very weak dependence on metallicity. Generally, the [Ce/ $\alpha$ ] ratios show this weak dependence, with the majority having slopes around  $0.03 \text{ dex Gyr}^{-1}$ . The study conducted by Jofré et al. (2020) yielded comparable values, finding an equivalent slope to ours concerning [Ce/Si], along with a minor variation of  $0.007 \text{ dex Gyr}^{-1}$  for [Ce/Mg].

The traits that involve Zr, which have the strongest metallicity dependence, have quite weak correlation factor for the most metal-poor group. It is thus possible that our Zr measurements are simply very uncertain at low [Fe/H]. A similar effect might be causing the poor correlation found for Nd. We know that Nd lines are strong and heavily affected by hyperfine structure splitting, causing a large line-to-line scatter in abundance measurements (Casamiquela et al. 2020). It is interesting that the classical [Y/Mg] trait is not the element with the strongest correlation coefficient, or the weakest dependence in metallicity. The trait that is the best candidate for chemical clock seems to be [Ce/Ca], followed by [Ce/Al] (see Figs. 12 and 13, respectively) because of their strength of the slope and weak metallicity dependence. Another ratio displaying similar characteristics is [Ce/Eu], even though from Fig. 13 we can see that its overall trend with age is very flat, thus not making this element ratio vary much with time. Sales-Silva et al. (2022) tested the [Ce/ $\alpha$ ] ratios as stellar chemical clocks by examining the evolution of Ce in 42 open clusters. Their conclusion suggests that these ratios exhibit variability across the disk owing to the influence of AGB yields, which are dependent on metallicity. It should be

noted, however, that the clusters analyzed in their study encompass a wider Galactic radius ( $6 \lesssim R_{GC} \lesssim 20 \text{ kpc}$ ) compared to our work. At the same time, their analysis revealed a comparable age-dependence pattern within two distinct metallicity groups (namely  $-0.6 < [\text{Fe}/\text{H}] < -0.1$  and  $-0.1 < [\text{Fe}/\text{H}] < +0.4$ ), which is a similar to the behavior observed in our relations. The study of 47 open clusters conducted by Casamiquela et al. (2021) also revealed an increasing scatter in the age-abundance relations across various radii outside the solar neighborhood ( $d > 1 \text{ kpc}$ ), demonstrating a dependence on the spatial volume analyzed. However, they did not consider in particular ratios involving Ce.

Accounting for all the astrophysical explanations, deriving robust conclusions solely based on pure metallicity dependence becomes challenging due to the dispersion in abundance-age trends. Factors beyond chemical evolution arguments can significantly impact these relations, and complicate the comprehension of our chemical trends. These variables might include uncertainties associated with determining atmospheric parameters (partly due to the level of the S/N of the measurements) and inaccuracies in estimating the ages for giant stars (Hayden et al. 2022; Sharma et al. 2022).

Another aspect to consider concerns the use of linear fittings that can potentially constrain the interpretation of the data, particularly when dealing with older stars. Due to their increased dispersion, linear regressions may no longer accurately capture their trends. To best reproduce the different chemical-age features, as turnovers or varying slopes across age ranges, Spina et al. (2016) explored hyperbolic and two-segmented line fits in their study, while Casali et al. (2020) used a multivariate linear regression, incorporating metallicity as a dimension. Along the same lines, Delgado Mena et al. (2017) fit different multidimensional relations to the abundance-age trends analyzed in their work. These attempts highlight that employing fitting models beyond linear regression could offer an alternative to replicate the observed tagging trends. Nevertheless, employing higher-order polynomials might also introduce additional complexity, making it more challenging to interpret the results and to disentangle the various dependences.

To account for multiple dependences, different approaches and more sophisticated techniques have recently been developed. One example is the work of Hayden et al. (2022), who used a machine learning algorithm to infer ages.

Subsequently, [Sharma et al. \(2022\)](#), in a related study, used these same ages to investigate 2D relationships between stellar ages, metallicities, and various combinations of  $[X/Fe]$  ratios. Another recent effort by [Prantzos et al. \(2023\)](#) utilized 1D semi-analytical models in conjunction with high-resolution data to explore the optimal combination of  $[X/Y]$  for tracing the evolution of thick and thin disks.

## 5. Discussion

Despite the extensive exploration of chemical tagging in recent years, there are still open questions to be addressed. For instance, which traits show the strongest dependence on metallicity and how do we explain these dependences from the point of view of Galactic evolution. Ultimately, in the complex scenario of chemical trends, we wonder whether it is feasible to pinpoint “golden” candidates for chemical tagging?

### 5.1. Assumptions and implications in Galactic evolution

Given the extended metallicity and age ranges covered by our sample, we were able to explore various abundance ratios at different metallicities. As outlined in other studies (e.g., [Feltzing et al. 2017](#); [Delgado Mena et al. 2019](#); [Casali et al. 2020](#); [Magrini et al. 2021](#)), we observed a non-uniform pattern in the relationship between abundance and age, attributed to variations in metallicity. Specifically, we observed a diminishing trend in the correlation between stellar ages and  $[Fe/H]$  values, indicative of decreasing age precision with changing metallicity.

This behavior needs to be considered when pursuing chemical tagging, particularly for individual field stars. The dependence on metallicity poses a constraint on the possibility of using the chemical-age relation within the context of Galactic archaeology. Leveraging observed abundance patterns to constrain chemical enrichment history and infer stellar ages can serve as a potent tool, but requires consideration from various perspectives.

First, if we assume that stars of a specific age retain the characteristics of their original gas, which should remain chemically distinct, then the chemical space enables dating the star and its hosting environment. However, this notion becomes less straightforward when considering that stars possess different birth radii, being born in different places.

Focusing on the metallicity dependence, and despite the assumption that the heritability of stars descending from the same gas cloud can be retrieved by chemical abundances, it is essential to note that the complexity of the combination of production sites of the elements and the different Galactic locations where the stars are born can render this picture less straightforward to interpret. The abundances analyzed in this work come from a variety of sources that act on different timescales according to the theory of Galactic evolution ([Freeman & Bland-Hawthorn 2002](#); [Rix & Bovy 2013](#); [Matteucci 2016](#)). As discussed in Sect. 4.4, certain nucleosynthesis processes and their associated yields, particularly for AGBs, are subject to the influence of the source’s metallicity. This dependence will inevitably impact the production of various elements, leading in the final production to the prevalence of certain elements over others, for example in the first-peak and second-peak n-capture elements.

Alongside the diversity of production channels, it is important to add to the picture the intricate diversity of chemical substructures within our Galaxy, which suggests the presence of a complex mixture of stellar populations. The ISM will be enriched differently according to the star formation rate and star

formation history characterizing the Galactic volume considered. This stochastic enrichment ([Krumholz & Ting 2018](#)) grows more intricate when adding the role of stellar migration in blurring chemical gradients and signatures as stars from different sites mix together. The variations in the chemical clock relations are notably influenced by the diverse birth radii of stars ([Sellwood & Binney 2002](#); [Minchev et al. 2012](#)), which in their abundances carry the fingerprints of distinct local star formation histories, as demonstrated by the recent work by [Ratcliffe et al. \(2024\)](#).

In our case the stellar sample is composed of field stars. Although their positions place them in the solar neighborhood (see Fig. 1), it cannot be ruled out that they might have travelled across the Galactic disk. The spread in the age-metallicity relation (Fig. 7) and the presence of solar metallicity stars with ages of  $\sim 10$  Gyr suggests that those older stars might have formed in the inner Galaxy and then migrated radially toward the solar neighborhood. In such instances, the dispersion in the chemical-age relations could potentially be attributed to differences in birth radii (and consequently different local metallicity) that trace the composition of the original ISM. A star formed in an ISM with lower iron content undergoes a diminished supply of iron for neutron capture processes ([Karakas & Lugaro 2016](#); [Cescutti & Matteucci 2022](#)), hence diminishing the production of n-capture elements and weakening the  $[n\text{-capture}/\alpha]$ -age trends.

Second, through the analysis with two known chemical clocks mostly employed for solar analog stars (see Sect. 4.3), we found that these ratios for the solar group continue to serve as reliable indicators of chemical enrichment, also in the case of our more evolved targets, such as giant stars. This aligns with the results presented by [Slumstrup et al. \(2017\)](#), who confirmed the tight correlation between  $[Y/Mg]$  and age for six evolved stars. [Berger et al. \(2022\)](#) recovered a significant trend for nonsolar FGK stars, even if less precise than the relations inferred for solar analogs. Moreover, most of the coefficients of the solar group (see Table B.1) are in good agreement with those found by [Jofré et al. \(2020\)](#), with the exception of Zr and Al which show greater slopes in our work.

Hence, by confining the analysis to the solar metallicity range, the chemical-age relations appear relatively consistent between red giant and main-sequence stars, and thus are not dependent on detailed stellar evolution. While we acknowledge the possibility that the poorly understood mixing processes occurring in evolved stars ([Mosser et al. 2014](#)) can alter the stellar compositions, these mechanisms do not appear to erase the correlation between age and  $\alpha$ -capture and n-capture elements for giant stars, making them valuable for Galactic archaeology studies.

### 5.2. Limitation and caveats

When using chemical stellar dating, other variables might cause the variations in the different  $[X/Y]$ -age planes. Disentangling the scatter due to astrophysical origin from the scatter caused by method uncertainties is not trivial. The situation becomes more severe in the low-metallicity regime, where the age predictability of the chemical clocks decreases.

The systematic average internal uncertainties of  $\sim 0.03$  dex for  $[Y/Mg]$  and  $[Y/Al]$  (see Fig. 11) is smaller than the scatter around the linear fit for each metallicity group, ranging from 0.05 to 0.15 dex. This means that the observed dispersion around the linear fit cannot be accounted for only by the internal precision. Other factors that affect the abundance measurements can be errors from atomic diffusion, molecular data, omission of NLTE corrections, and 3D effects ([Adibekyan et al. 2015](#); [Storm & Bergemann 2023](#); [Alexeeva et al. 2023](#)), as well as



the reliance on the chosen lines for abundance measurement (Nissen & Gustafsson 2018; Jofré et al. 2019; Slumstrup et al. 2019). All these external factors are partially responsible in the spread seen in the chemical-age trends. The situation described above highlights the importance of having accurate and precise age and abundance estimations when studying chemical trends in the context of Galactic evolution.

### 5.3. Exploring the best chemical traits

Despite the above-mentioned factors, through our analysis we once again reveal the age-related information conveyed by the *s*-process over  $\alpha$  elements. Owing to their different nucleosynthesis processes and production timescales, the change with time is strongly correlated to their element ratios, as can be seen in Fig. 9. We confirm that the most significant correlation is evident in stars with solar-metallicity, gradually weakening in stars with lower [Fe/H].

When examining the metallicity dependence of the various combinations, we see that some *n*-capture elements such as Zr, Sr, and Y display considerable differences in the slopes, as can be seen in Fig. 14. Therefore, we believe that, even when these elements display steep slopes and high correlation coefficients with age, their sensitivity to stellar metallicity implies their lack of universality. Nevertheless, they can be used for specific metallicity ranges, or their measurements could potentially be improved by relying on a greater number of lines for their abundances. Other abundance ratios display low dependences in metallicity, but also small  $\rho$  values, such as ratios involving Nd, thus failing to encompass age-related information within their trends. The combinations of [*s/r*]-process elements ratios also exhibit low dependences on [Fe/H], but of the values of the slopes in Table B.1 only the slope for [Zr/Eu] is greater than the threshold value, that is 0.03 dex Gyr<sup>-1</sup>. On the other hand, ratios such as [Ce/Al] and [Ce/Ti], although they show a weak dependence on metallicity, are related with age with slopes greater than 0.03 dex Gyr<sup>-1</sup>, showing higher correlation coefficients. On the whole, ratios comprising Ce at numerators generally have lower metallicity dependence, making them potentially reliable and consistent chemical clocks.

From these results identifying an ideal candidate for chemical clocks is not straightforward; our analysis leans toward ratios exhibiting slopes steep enough to retrieve age information, but at the same time with weak dependence on metallicity. Even so, the selection of one element combination over another relies on the precision attainable for each specific element. This depends on factors such as the spectral type of the star, the precision at which we can measure atmospheric parameters and abundance, and the number of measurable lines. We note that in this analysis we excluded iron-peak elements as we chose to prioritize examining the dependence on iron, hence not exploring all the possible combinations of chemical traits.

## 6. Conclusion

No universally optimal abundance ratios for chemically dating stars have emerged. This lack of universality spans across different metallicities (as discovered here and in various studies, e.g., Feltzing et al. 2017; Delgado Mena et al. 2017) and positions (Titarenko et al. 2019; Casali et al. 2020). We suggest that the selection criteria should be contingent upon the metallicity range of the stars. Within this context, our analysis offers a method of disentangling the dependence on metallicity by examining the efficacy of various element ratios in retrieving age information within specific metallicity ranges. It has been demonstrated that

certain ratios are applicable at solar metallicity, exhibiting more pronounced age-related patterns, but they lose their age correlations when applied to stars with lower iron content. Others can be regarded as golden ratios because they consistently hold true across all metallicities. As an example, the combination of Zr over  $\alpha$  elements can be used for solar metallicity stars, but proves less effective for most metal-poor stars, as their slopes in the [X/Y]-age trend weaken. On the other hand, ratios with Ce and La appear to be easily usable at different ranges of metallicities, being more independent on the stellar iron content. Additionally, when selecting chemical candidates, factors such as measurement precision, the type of star (which significantly impacts age determination), and the spatial coverage of the sample should be kept in mind. Although we did not find consistency in the various chemical clocks for the different metallicity groups, we recovered [n-capture/ $\alpha$ ]-age trends with an internal abundance precision of <0.03 dex and a mean relative age uncertainty of around 20%.

Our exploration of different chemical ratios highlighted that the potential of chemical clocks extends beyond stellar dating. They can serve as valuable tools in identifying discrepancies in age estimation, especially in cases where stars might have previously been part of binary systems and subsequently accreted mass, as we speculate for two stars in our sample. This potential can be harnessed to detect such stars, which might otherwise remain hidden by a chemical analysis alone or within single evolutionary tracks that do not account for binary systems.

Notwithstanding the non-universality of chemical traits, abundance ratios remain a source of key information in Galactic archaeology. Thanks to the recent massive spectroscopic surveys and the revolutionary data from *Gaia* DR3 they enable us to build a chronological map of the Milky Way by linking chemistry and stellar ages.

*Acknowledgements.* We thank the anonymous referee for the useful comments that have improved this work. S.V. thanks ANID (Beca Doctorado Nacional, folio 21220489) and Universidad Diego Portales for the financial support provided. S.V. and P.J. acknowledge the Millennium Nucleus ERIS (ERIS NCN2021017) and FONDECYT (Regular number 1231057) for the funding. I express my gratitude to Theosamuele Signor for the valuable insights and the helpful discussions. This work has made use of data from the European Space Agency (ESA) mission *Gaia* (<https://www.cosmos.esa.int/gaia>), processed by the *Gaia* Data Processing and Analysis Consortium (DPAC, <https://www.cosmos.esa.int/web/gaia/dpac/consortium>). Funding for the DPAC has been provided by national institutions, in particular the institutions participating in the *Gaia* Multilateral Agreement.

## References

- Abdurro'uf, Accetta, K., Aerts, C., et al. 2022, *ApJS*, 259, 35  
 Adibekyan, V., Figueira, P., Santos, N. C., et al. 2015, *A&A*, 583, A94  
 Aguirre Børsen-Koch, V., Rørsted, J. L., Justesen, A. B., et al. 2022, *MNRAS*, 509, 4344  
 Alexeeva, S., Wang, Y., Zhao, G., et al. 2023, *ApJ*, 957, 10  
 Alvarez, R., & Plez, B. 1998, *A&A*, 330, 1109  
 Amarsi, A. M., Lind, K., Osorio, Y., et al. 2020, *A&A*, 642, A62  
 Anders, F., Chiappini, C., Rodrigues, T. S., et al. 2017, *A&A*, 597, A30  
 Anders, F., Gispert, P., Ratcliffe, B., et al. 2023, *A&A*, 678, A158  
 Andrievsky, S. M., Spite, M., Korotin, S. A., et al. 2007, *A&A*, 464, 1081  
 Arentoft, T., Grundahl, F., White, T. R., et al. 2019, *A&A*, 622, A190  
 Baratella, M., D'Orazi, V., Sheminova, V., et al. 2021, *A&A*, 653, A67  
 Bergemann, M., Lind, K., Collet, R., & Asplund, M. 2011, *J. Phys. Conf. Ser.*, 328, 012002  
 Berger, T. A., van Saders, J. L., Huber, D., et al. 2022, *ApJ*, 936, 100  
 Bisterzo, S., Pompeia, L., Gallino, R., et al. 2005, *Nucl. Phys. A*, 758, 284  
 Bisterzo, S., Travaglio, C., Gallino, R., Wiescher, M., & Käppeler, F. 2014, *ApJ*, 787, 10  
 Blanco-Cuaresma, S. 2019, *MNRAS*, 486, 2075  
 Blanco-Cuaresma, S., Soubiran, C., Heiter, U., & Jofré, P. 2014a, *A&A*, 569, A111



- Blanco-Cuaresma, S., Soubiran, C., Jofré, P., & Heiter, U. 2014b, *A&A*, **566**, A98
- Bland-Hawthorn, J., Sharma, S., Tepper-García, T., et al. 2019, *MNRAS*, **486**, 1167
- Bovy, J., Rix, H.-W., Liu, C., et al. 2012, *ApJ*, **753**, 148
- Brogaard, K., Jessen-Hansen, J., Handberg, R., et al. 2016, *Astron. Nachr.*, **337**, 793
- Brown, T. M., Gilliland, R. L., Noyes, R. W., & Ramsey, L. W. 1991, *ApJ*, **368**, 599
- Buder, S., Sharma, S., Kos, J., et al. 2021, *MNRAS*, **506**, 150
- Casali, G., Spina, L., Magrini, L., et al. 2020, *A&A*, **639**, A127
- Casamiquela, L., Tarricq, Y., Soubiran, C., et al. 2020, *A&A*, **635**, A8
- Casamiquela, L., Soubiran, C., Jofré, P., et al. 2021, *A&A*, **652**, A25
- Cescutti, G., & Matteucci, F. 2022, *Universe*, **8**, 173
- Chaplin, W. J., & Miglio, A. 2013, *ARA&A*, **51**, 353
- Chaplin, W. J., Basu, S., Huber, D., et al. 2014, *ApJS*, **210**, 1
- Chiappini, C., Matteucci, F., & Gratton, R. 1997, *ApJ*, **477**, 765
- Côté, B., Fryer, C. L., Belczynski, K., et al. 2018, *ApJ*, **855**, 99
- Cristallo, S., Straniero, O., Piersanti, L., & Gobrecht, D. 2015, *ApJS*, **219**, 40
- Cutri, R. M., Skrutskie, M. F., van Dyk, S., et al. 2003, *VizieR Online Data Catalog: II/246*
- da Silva, R., Porto de Mello, G. F., Milone, A. C., et al. 2012, *A&A*, **542**, A84
- Das, P., Hawkins, K., & Jofré, P. 2020, *MNRAS*, **493**, 5195
- Delgado Mena, E., Tsantaki, M., Adibekyan, V. Z., et al. 2017, *A&A*, **606**, A94
- Delgado Mena, E., Moya, A., Adibekyan, V., et al. 2019, *A&A*, **624**, A78
- Deng, L.-C., Newberg, H. J., Liu, C., et al. 2012, *Res. Astron. Astrophys.*, **12**, 735
- De Silva, G. M., Freeman, K. C., Bland-Hawthorn, J., et al. 2015, *MNRAS*, **449**, 2604
- Feltzing, S., Howes, L. M., McMillan, P. J., & Stokutė, E. 2017, *MNRAS*, **465**, L109
- Feuillet, D. K., Bovy, J., Holtzman, J., et al. 2018, *MNRAS*, **477**, 2326
- Feuillet, D. K., Frankel, N., Lind, K., et al. 2019, *MNRAS*, **489**, 1742
- Fischler, M. A., & Bolles, R. C. 1981, *Commun. ACM*, **24**, 381
- François, P., Matteucci, F., Cayrel, R., et al. 2004, *A&A*, **421**, 613
- Frankel, N., Sanders, J., Ting, Y.-S., & Rix, H.-W. 2020, *ApJ*, **896**, 15
- Freeman, K., & Bland-Hawthorn, J. 2002, *ARA&A*, **40**, 487
- Fujimoto, Y., Krumholz, M. R., & Inutsuka, S.-i. 2020, *MNRAS*, **497**, 2442
- Gaia Collaboration (Prusti, T., et al.) 2016, *A&A*, **595**, A1
- Gaia Collaboration (Valenari, A., et al.) 2023, *A&A*, **674**, A1
- Gallino, R., Bisterzo, S., Straniero, O., Ivans, I. I., & Käppeler, F. 2006, *Mem. Soc. Astron. It.*, **77**, 786
- Gilliland, R. L., Brown, T. M., Christensen-Dalsgaard, J., et al. 2010, *PASP*, **122**, 131
- Gilmore, G., Randich, S., Asplund, M., et al. 2012, *Messenger*, **147**, 25
- Goswami, A., Shejeelammal, J., Goswami, P. P., & Purandardas, M. 2024, *Bull. Soc. Roy. Sci. Liège*, **93**, 406
- Green, G. M., Schlafly, E., Zucker, C., Speagle, J. S., & Finkbeiner, D. 2019, *ApJ*, **887**, 93
- Gustafsson, B., Edvardsson, B., Eriksson, K., et al. 2008, *A&A*, **486**, 951
- Hawkins, K., Jofré, P., Masseron, T., & Gilmore, G. 2015, *MNRAS*, **453**, 758
- Hayden, M. R., Sharma, S., Bland-Hawthorn, J., et al. 2022, *MNRAS*, **517**, 5325
- Hegedűs, V., Mészáros, S., Jofré, P., et al. 2023, *A&A*, **670**, A107
- Heiter, U., Jofré, P., Gustafsson, B., et al. 2015, *A&A*, **582**, A49
- Heiter, U., Lind, K., Bergemann, M., et al. 2021, *A&A*, **645**, A106
- Hidalgo, S. L., Pietrinferni, A., Cassisi, S., et al. 2018, *ApJ*, **856**, 125
- Hirai, Y., Saitoh, T. R., Ishimaru, Y., & Wanajo, S. 2018, *ApJ*, **855**, 63
- Hogg, D. W., Casey, A. R., Ness, M., et al. 2016, *ApJ*, **833**, 262
- Howell, S. B., Sobek, C., Haas, M., et al. 2014, *PASP*, **126**, 398
- Huber, D., Bryson, S. T., Haas, M. R., et al. 2016, *ApJS*, **224**, 2
- Izzard, R. G., Preece, H., Jofre, P., et al. 2018, *MNRAS*, **473**, 2984
- Jofré, P. 2021, *ApJ*, **920**, 23
- Jofré, P., Das, P., Bertranpetit, J., & Foley, R. 2017, *MNRAS*, **467**, 1140
- Jofré, P., Heiter, U., & Soubiran, C. 2019, *ARA&A*, **57**, 571
- Jofré, P., Jackson, H., & Tucci Maia, M. 2020, *A&A*, **633**, L9
- Jofré, P., Jorissen, A., Aguilera-Gómez, C., et al. 2023, *A&A*, **671**, A21
- Jönsson, H., Holtzman, J. A., Allende Prieto, C., et al. 2020, *AJ*, **160**, 120
- Karakas, A. I., & Lattanzio, J. C. 2014, *PASA*, **31**, e030
- Karakas, A. I., & Lugaro, M. 2016, *ApJ*, **825**, 26
- Kitaura, F. S., Janka, H. T., & Hillebrandt, W. 2006, *A&A*, **450**, 345
- Kjeldsen, H., & Bedding, T. R. 1995, *A&A*, **293**, 87
- Kobayashi, C., Umeda, H., Nomoto, K., Tominaga, N., & Ohkubo, T. 2006, *ApJ*, **653**, 1145
- Kobayashi, C., Karakas, A. I., & Lugaro, M. 2020, *ApJ*, **900**, 179
- Krumholz, M. R., & Ting, Y.-S. 2018, *MNRAS*, **475**, 2236
- Leung, H. W., Bovy, J., Mackey, J. T., & Miglio, A. 2023, *MNRAS*, **522**, 4577
- Liu, S., Shi, J., & Wu, Z. 2020, *ApJ*, **896**, 64
- Lugaro, M., Herwig, F., Lattanzio, J. C., Gallino, R., & Straniero, O. 2003, *ApJ*, **586**, 1305
- Magrini, L., Sestito, P., Randich, S., & Galli, D. 2009, *A&A*, **494**, 95
- Magrini, L., Spina, L., Randich, S., et al. 2018, *A&A*, **617**, A106
- Magrini, L., Vescovi, D., Casali, G., et al. 2021, *A&A*, **646**, L2
- Majewski, S. R., Schiavon, R. P., Frinchaboy, P. M., et al. 2017, *AJ*, **154**, 94
- Martig, M., Rix, H.-W., Silva Aguirre, V., et al. 2015, *MNRAS*, **451**, 2230
- Mashonkina, L., Sitnova, T., Yakovleva, S. A., & Belyaev, A. K. 2019, *A&A*, **631**, A43
- Matteucci, F. 2012, *Chemical Evolution of Galaxies* (Astronomy and Astrophysics Library)
- Matteucci, F. 2016, *J. Phys. Conf. Ser.*, **703**, 012004
- Matteucci, F., Raiteri, C. M., Busson, M., Gallino, R., & Gratton, R. 1993, *A&A*, **272**, 421
- Miglio, A. 2012, in *Red Giants as Probes of the Structure and Evolution of the Milky Way*, Astrophysics and Space Science Proceedings, **26**, 11
- Miglio, A., Chaplin, W. J., Brogaard, K., et al. 2016, *MNRAS*, **461**, 760
- Minchev, I., & Famaey, B. 2010, *ApJ*, **722**, 112
- Minchev, I., Famaey, B., Quillen, A. C., et al. 2012, *A&A*, **548**, A126
- Minchev, I., Steinmetz, M., Chiappini, C., et al. 2017, *ApJ*, **834**, 27
- Mosser, B., Benomar, O., Belkacem, K., et al. 2014, *A&A*, **572**, L5
- Nissen, P. E. 2015, *A&A*, **579**, A52
- Nissen, P. E. 2016, *A&A*, **593**, A65
- Nissen, P. E., & Gustafsson, B. 2018, *A&ARv*, **26**, 6
- Nissen, P. E., Silva Aguirre, V., Christensen-Dalsgaard, J., et al. 2017, *A&A*, **608**, A112
- Nissen, P. E., Christensen-Dalsgaard, J., Mosumgaard, J. R., et al. 2020, *A&A*, **640**, A81
- Noels, A., & Bragaglia, A. 2015, in *Asteroseismology of Stellar Populations in the Milky Way*, Astrophys. Space Sci. Proc., **39**, 167
- Ou, X., Roederer, I. U., Sneden, C., et al. 2020, *ApJ*, **900**, 106
- Pietrinferni, A., Hidalgo, S., Cassisi, S., et al. 2021, *ApJ*, **908**, 102
- Pignatari, M., Gallino, R., Heil, M., et al. 2010, *ApJ*, **710**, 1557
- Pinsonneault, M. H., Elsworth, Y., Epstein, C., et al. 2014, *ApJS*, **215**, 19
- Plez, B. 2012, Astrophysics Source Code Library [record ascl:1205.004]
- Prantzos, N., Abia, C., Chen, T., et al. 2023, *MNRAS*, **523**, 2126
- Preston, G. W., & Sneden, C. 2000, *AJ*, **120**, 1014
- Ratcliffe, B. L., Ness, M. K., Johnston, K. V., & Sen, B. 2020, *ApJ*, **900**, 165
- Ratcliffe, B., Minchev, I., Anders, F., et al. 2023, *MNRAS*, **525**, 2208
- Ratcliffe, B., Minchev, I., Cescutti, G., et al. 2024, *MNRAS*, **528**, 3464
- Recio-Blanco, A., Fernández-Alvar, E., de Laverny, P., et al. 2021, *A&A*, **648**, A108
- Reddy, A. B. S., & Lambert, D. L. 2017, *ApJ*, **845**, 151
- Rendle, B. M., Miglio, A., Chiappini, C., et al. 2019, *MNRAS*, **490**, 4465
- Rix, H.-W., & Bovy, J. 2013, *A&ARv*, **21**, 61
- Sahlholdt, C. L., & Silva Aguirre, V. 2018, *MNRAS*, **481**, L125
- Sahlholdt, C. L., Feltzing, S., & Feuillet, D. K. 2022, *MNRAS*, **510**, 4669
- Sales-Silva, J. V., Dafon, S., Cunha, K., et al. 2022, *ApJ*, **926**, 154
- Sandage, A. R. 1953, *AJ*, **58**, 61
- Schlafly, E. F., & Finkbeiner, D. P. 2011, *ApJ*, **737**, 103
- Sellwood, J. A., & Binney, J. J. 2002, *MNRAS*, **336**, 785
- Serenelli, A., Johnson, J., Huber, D., et al. 2017, *ApJS*, **233**, 23
- Sharma, S., Stello, D., Buder, S., et al. 2018, *MNRAS*, **473**, 2004
- Sharma, S., Hayden, M. R., Bland-Hawthorn, J., et al. 2022, *MNRAS*, **510**, 734
- Silva Aguirre, V., Casagrande, L., Basu, S., et al. 2012, *ApJ*, **757**, 99
- Silva Aguirre, V., Davies, G. R., Basu, S., et al. 2015, *MNRAS*, **452**, 2127
- Silva Aguirre, V., Bojsen-Hansen, M., Slumstrup, D., et al. 2018, *MNRAS*, **475**, 5487
- Silva Aguirre, V., Stello, D., Stokholm, A., et al. 2020, *ApJ*, **889**, L34
- Slumstrup, D., Grundahl, F., Brogaard, K., et al. 2017, *A&A*, **604**, L8
- Slumstrup, D., Grundahl, F., Silva Aguirre, V., & Brogaard, K. 2019, *A&A*, **622**, A111
- Spina, L., Meléndez, J., Karakas, A. I., et al. 2016, *A&A*, **593**, A125
- Spina, L., Meléndez, J., Karakas, A. I., et al. 2018, *MNRAS*, **474**, 2580
- Stello, D., Vandenberg, A., Casagrande, L., et al. 2016, *ApJ*, **832**, 133
- Stokholm, A., Aguirre Børsen-Koch, V., Stello, D., Hon, M., & Reyes, C. 2023, *MNRAS*, **524**, 1634
- Storm, N., & Bergemann, M. 2023, *MNRAS*, **525**, 3718
- Tautvaišienė, G., Viscasillas Vázquez, C., Mikolaitis, Š., et al. 2021, *A&A*, **649**, A126
- Titarenko, A., Recio-Blanco, A., de Laverny, P., Hayden, M., & Guiglion, G. 2019, *A&A*, **622**, A59
- Travaglio, C., Gallino, R., Arnone, E., et al. 2004, *ApJ*, **601**, 864
- Tucci Maia, M., Ramírez, I., Meléndez, J., et al. 2016, *A&A*, **590**, A32
- Valentini, M., Chiappini, C., Miglio, A., et al. 2016, *Astron. Nachr.*, **337**, 970
- Viscasillas Vázquez, C., Magrini, L., Casali, G., et al. 2022, *A&A*, **660**, A135
- Walsen, K., Jofré, P., Buder, S., et al. 2024, *MNRAS*, **529**, 2946
- Zenati, Y., Perets, H. B., Dessart, L., et al. 2023, *ApJ*, **944**, 22

## Appendix A: Target information

**Table A.1.** The EPIC (K2) IDs are listed in the first column for the entire sample. Subsequently, the *Gaia* IDs along with their corresponding coordinates (RA and DEC) and *G* magnitudes are presented. The signal-to-noise ratios (S/N) are presented in the sixth column. The asteroseismic frequency separation  $\Delta\nu$ , together with the frequency of maximum power  $\nu_{max}$  were obtained from the K2 catalogue. Finally the 2MASS magnitudes are reported in J, H and K bands. The two stars likely parts of binary systems are not listed in the table.

EPIC ID	<i>Gaia</i> DR3 ID	RA	DEC	<i>G</i> <sub>mag</sub>	S/N	$\Delta\nu$	$\nu_{max}$	<i>J</i> <sub>mag</sub>	<i>H</i> <sub>mag</sub>	<i>K</i> <sub>mag</sub>
212328705	3603874691200483584	204.108972	-16.70291629	9.56	97	5.63	56.38	7.95	7.41	7.28
201387934	3791659118172624512	169.8884225	-1.143003424	9.88	94	4.31	35.09	8.29	7.76	7.61
201610179	3810779934617363584	170.7994691	2.201317576	9.54	94	8.43	93.78	8.05	7.59	7.46
201615553	3810802165368121984	171.0301093	2.283891994	9.56	93	3.73	33.54	7.94	7.43	7.29
201436971	3797212025554640640	173.1636164	-0.406484518	9.95	92	5.72	58.86	8.31	7.78	7.64
206049832	2601007287942620032	338.6186258	-13.42684939	9.64	92	1.8	34.01	8.09	7.55	7.45
210729904	47764610473398016	64.89874585	18.80338613	10.25	91	14.27	251.11	8.36	7.8	7.66
205989874	2599221543620591232	336.0198833	-15.12118093	9.37	91	3.45	26.76	7.84	7.33	7.22
210875646	51670728611455360	58.95835214	21.01350234	10.49	90	0.82	4.25	8.29	7.49	7.34
205935544	2595016839357041664	337.9320516	-16.85770001	10.38	90	4.14	30.29	8.88	8.44	8.26
206166172	2614051064966374784	332.5811764	-10.40084002	10.11	90	6.0	58.19	8.51	7.94	7.81
210557561	46220449471982208	60.49102134	16.3313616	9.61	90	5.48	56.08	7.68	7.08	6.92
201504843	3796029608173623296	177.2799633	0.596013632	11.3	89	14.27	188.58	9.95	9.52	9.45
206057733	2600597681206509824	334.3914421	-13.21705184	10.56	89	6.98	74.18	9.07	8.57	8.44
201834045	381702722247093760	169.2843704	5.997252977	11.37	89	4.67	44.29	9.68	9.1	8.98
211006381	52907060716766080	63.16466585	23.07606484	10.23	88	3.61	32.3	7.86	7.13	6.93
210904019	63700485331065472	57.41907273	21.4528989	10.17	88	1.44	9.74	8.26	7.6	7.43
201801438	3813366776239786112	172.7488947	5.39292346	10.38	88	7.44	71.93	8.79	8.35	8.18
201584294	3796479514587811072	177.0167383	1.800451943	10.23	88	4.82	43.74	8.54	7.94	7.82
201380381	3794078971466576768	173.3835933	-1.25747885	10.47	88	7.17	73.28	8.97	8.42	8.36
201695150	3800805366992735360	174.0922748	3.557615343	9.5	87	9.94	109.25	7.97	7.47	7.34
206012087	2599468860721809408	335.9863649	-14.47835686	9.48	87	5.76	59.82	7.93	7.42	7.3
210329876	3304805952194320256	59.77071415	11.64807462	9.55	86	4.16	32.95	7.65	7.05	6.9
205991527	2599236971143099648	335.7188622	-15.06953592	9.37	86	4.65	41.69	7.71	7.17	7.03
211015044	53665345782804480	63.08209558	23.21443206	10.4	86	2.8	30.12	8.34	7.71	7.56
201798083	3813371964560265856	172.451626	5.332099278	9.83	86	3.63	29.84	8.19	7.62	7.47
210977032	65359510938866048	59.173947	22.616157	10.04	85	7.44	71.93	8.88	8.35	8.18
210724982	57497693561981952	51.56661758	18.73063083	9.86	85	4.73	40.4	8.33	7.82	7.74
210990463	53626622358017920	62.46723912	22.82266847	10.79	85	3.04	34.42	8.81	8.22	8.07
211083040	65991936282836864	60.31149905	24.29785844	10.78	84	5.12	46.84	9.12	8.6	8.51
211091343	66218951074368512	59.40521966	24.42591654	9.81	84	1.8	15.06	7.92	7.26	7.13
205953136	2596385074203302528	340.4845892	-16.26738208	10.99	83	4.81	44.09	9.4	8.78	8.61
211108599	66103845951674112	60.77734577	24.70042008	9.99	83	6.69	71.92	8.18	7.66	7.52
210480597	40016455113058560	59.70249644	15.07969951	9.94	83	1.92	14.61	7.79	7.15	6.93
210982421	52859541198660480	63.14881434	22.70042056	9.62	83	3.83	38.41	7.63	7.04	6.9
210578532	46279857459569664	60.67986033	16.64887014	9.79	82	1.61	11.15	7.65	7.0	6.82

Table A.2. Table A.1 continued.

EPIC ID	<i>Gaia</i> DR3 ID	RA	DEC	$G_{\text{mag}}$	S/N	$\Delta_{\nu}$	$\nu_{\text{max}}$	$J_{\text{mag}}$	$H_{\text{mag}}$	$K_{\text{mag}}$
211120167	66685453242145792	58.61152019	24.89475755	9.95	81	4.38	38.44	8.32	7.76	7.64
201393756	3797665612756053888	170.0989951	-1.055593065	10.97	81	4.97	46.2	9.36	8.85	8.67
211032114	148965309961550720	64.4060835	23.4813859	9.67	81	5.41	58.97	7.78	7.28	7.09
211029152	53722417308529792	62.11758335	23.43338483	10.72	79	7.68	43.09	8.41	7.64	7.42
211100795	66612404438442752	58.7373428	24.57405031	9.78	79	7.3	75.15	8.09	7.55	7.41
212323768	3605133498870789120	205.278068	-16.84117728	11.28	79	2.32	15.59	9.53	8.89	8.81
206218229	2608958401983554816	339.5905542	-9.469920682	9.76	79	4.9	44.75	8.03	7.47	7.27
203478307	6043454739975673344	243.1821768	-26.00487066	10.83	79	5.12	45.23	8.84	8.22	8.1
203367145	6235380954236279552	239.6732505	-26.37878524	10.2	79	4.69	42.57	8.41	7.85	7.73
211044578	149027466728165504	63.9129976	23.68320126	9.87	78	4.71	38.77	7.86	7.3	7.13
201531324	3796185154709476608	177.612019	1.006774282	9.29	78	3.64	31.58	7.87	7.35	7.24
210780208	57845345394803456	52.12542368	19.56914201	10.7	78	4.45	43.41	8.88	8.3	8.15
206509377	2626530320077918464	335.1881504	-4.687467974	9.9	77	4.45	37.76	8.31	7.8	7.67
201473281	3804057176928023168	168.3857731	0.120790002	9.97	77	16.02	214.69	8.54	8.03	7.91
206120536	2613677127933423744	330.7351883	-11.56185003	9.23	76	5.24	54.36	7.65	7.1	7.0
205929054	6825961802359128576	334.1660451	-17.08712916	11.17	76	7.2	72.63	9.73	9.24	9.09
211039480	53690978147432960	62.96880068	23.60085938	10.39	76	7.24	87.93	8.61	8.12	7.94
210976157	64078992209400064	58.0044248	22.60290508	10.47	74	4.29	37.92	8.56	7.95	7.8
201799986	3813361381760859392	172.623422	5.366302365	9.85	73	1.39	8.59	8.18	7.58	7.49
206322548	2622263214234941184	336.4938927	-7.887875111	11.66	72	4.63	26.75	10.2	9.71	9.58
206187923	2608825739033972224	339.0435866	-9.96799251	9.84	71	18.46	221.03	8.28	7.81	7.65
210977788	52834080632668288	63.34477847	22.62833215	10.87	70	4.24	39.13	8.74	8.13	7.92
210995892	65417372735307904	59.25809294	22.91023579	11.09	70	3.31	27.56	9.25	8.64	8.49
210964487	52802126076038272	63.03918788	22.41391435	9.95	70	3.52	26.71	7.74	7.08	6.86
201741868	3800997304787056256	174.1671701	4.345257611	11.42	70	5.66	56.13	9.8	9.23	9.11
211017969	148983898578548224	63.7152624	23.25812944	11.64	69	4.34	34.07	9.57	8.98	8.79
203848638	6034822646009063040	253.1051686	-24.7023971	10.09	69	6.48	59.12	8.39	7.85	7.76
203722894	6049568265144531456	243.3517865	-25.16200543	10.95	69	4.4	35.95	9.09	8.5	8.33
204640114	6243730920412078976	242.0595416	-21.5012362	10.52	69	2.12	28.31	8.63	8.01	7.85
203829170	6049773251041967360	242.5593522	-24.77676238	11.13	67	5.11	48.07	9.4	8.82	8.65
203722894	6049568265144531456	243.3517865	-25.16200543	10.95	67	4.4	35.95	9.09	8.5	8.33
210744319	57706291534137856	51.40042643	19.02251796	10.71	67	3.16	29.13	9.03	8.46	8.37
206211780	2615277982503739904	334.7283482	-9.571356794	11.42	66	8.33	88.03	9.95	9.42	9.33
210922109	63742507291336448	57.34670246	21.73908703	9.68	66	4.7	44.72	7.72	7.1	6.94
201640625	3800313030597421696	172.3870992	2.672229331	12.01	65	6.28	59.03	10.44	9.89	9.79
212322695	3603646439458466176	204.8885046	-16.87068314	11.15	63	4.98	44.57	9.52	8.98	8.84
201456500	3794842788451115904	177.0677615	-0.12614963	10.86	22	2.84	26.89	9.26	8.61	8.5

## Appendix B: Linear fit coefficients

**Table B.1.** Linear regression fit coefficients for the three metallicity groups as defined in Table 2. The slopes and their sigmas are expressed in dex  $\text{Gyr}^{-1}$ . The  $\rho$  values indicate the Pearson correlation coefficients for each relation.

Ratio	Group	Slope	$\sigma_{\text{slope}}$	$\rho$	Ratio	Group	Slope	$\sigma_{\text{slope}}$	$\rho$	Ratio	Group	Slope	$\sigma_{\text{slope}}$	$\rho$
Sr/Mg	poor	-0.026	0.009	0.653	La/Ca	poor	-0.011	0.005	0.57	Y/V	poor	-0.008	0.006	0.337
Sr/Mg	mix	-0.039	0.012	0.785	La/Ca	mix	-0.023	0.002	0.861	Y/V	mix	-0.023	0.004	0.732
Sr/Mg	solar	-0.04	0.017	0.762	La/Ca	solar	-0.023	0.007	0.766	Y/V	solar	-0.036	0.012	0.776
Sr/Si	poor	-0.018	0.013	0.502	La/Ti	poor	-0.012	0.005	0.533	Y/Al	poor	-0.012	0.007	0.461
Sr/Si	mix	-0.035	0.01	0.783	La/Ti	mix	-0.027	0.003	0.86	Y/Al	mix	-0.03	0.006	0.758
Sr/Si	solar	-0.042	0.021	0.743	La/Ti	solar	-0.029	0.009	0.812	Y/Al	solar	-0.046	0.02	0.739
Sr/Ca	poor	-0.018	0.011	0.479	Ce/Mg	poor	-0.02	0.006	0.708	Zr/Eu	poor	-0.009	0.009	0.298
Sr/Ca	mix	-0.034	0.005	0.839	Ce/Mg	mix	-0.031	0.007	0.809	Zr/Eu	mix	-0.028	0.007	0.764
Sr/Ca	solar	-0.034	0.016	0.761	Ce/Mg	solar	-0.032	0.013	0.762	Zr/Eu	solar	-0.039	0.008	0.857
Sr/Ti	poor	-0.018	0.01	0.52	Ce/Si	poor	-0.013	0.005	0.647	Zr/V	poor	-0.006	0.01	0.191
Sr/Ti	mix	-0.038	0.007	0.834	Ce/Si	mix	-0.028	0.007	0.807	Zr/V	mix	-0.029	0.004	0.829
Sr/Ti	solar	-0.042	0.019	0.785	Ce/Si	solar	-0.031	0.012	0.763	Zr/V	solar	-0.063	0.02	0.87
Y/Mg	poor	-0.015	0.007	0.555	Ce/Ca	poor	-0.015	0.004	0.706	Zr/Al	poor	-0.012	0.008	0.453
Y/Mg	mix	-0.028	0.006	0.742	Ce/Ca	mix	-0.027	0.003	0.883	Zr/Al	mix	-0.034	0.007	0.82
Y/Mg	solar	-0.037	0.018	0.698	Ce/Ca	solar	-0.024	0.007	0.77	Zr/Al	solar	-0.068	0.025	0.876
Y/Si	poor	-0.007	0.005	0.404	Ce/Ti	poor	-0.016	0.006	0.647	La/Eu	poor	-0.012	0.007	0.52
Y/Si	mix	-0.027	0.005	0.765	Ce/Ti	mix	-0.031	0.003	0.871	La/Eu	mix	-0.019	0.007	0.658
Y/Si	solar	-0.038	0.017	0.658	Ce/Ti	solar	-0.031	0.01	0.806	La/Eu	solar	-0.012	0.003	0.696
Y/Ca	poor	-0.008	0.004	0.465	Nd/Mg	poor	-0.016	0.012	0.448	La/V	poor	-0.011	0.004	0.599
Y/Ca	mix	-0.024	0.003	0.814	Nd/Mg	mix	-0.02	0.006	0.634	La/V	mix	-0.021	0.004	0.801
Y/Ca	solar	-0.027	0.01	0.712	Nd/Mg	solar	-0.034	0.011	0.718	La/V	solar	-0.033	0.01	0.836
Y/Ti	poor	-0.01	0.004	0.445	Nd/Si	poor	-0.007	0.007	0.338	La/Al	poor	-0.017	0.006	0.595
Y/Ti	mix	-0.028	0.004	0.807	Nd/Si	mix	-0.016	0.005	0.65	La/Al	mix	-0.027	0.005	0.792
Y/Ti	solar	-0.034	0.014	0.764	Nd/Si	solar	-0.03	0.011	0.749	La/Al	solar	-0.038	0.013	0.814
Zr/Mg	poor	-0.014	0.006	0.597	Nd/Ca	poor	-0.008	0.005	0.397	Ce/Eu	poor	-0.015	0.006	0.642
Zr/Mg	mix	-0.033	0.008	0.803	Nd/Ca	mix	-0.015	0.003	0.741	Ce/Eu	mix	-0.023	0.007	0.715
Zr/Mg	solar	-0.061	0.021	0.84	Nd/Ca	solar	-0.024	0.005	0.811	Ce/Eu	solar	-0.013	0.004	0.691
Zr/Si	poor	-0.008	0.006	0.342	Nd/Ti	poor	-0.01	0.007	0.356	Ce/V	poor	-0.015	0.006	0.673
Zr/Si	mix	-0.032	0.004	0.845	Nd/Ti	mix	-0.018	0.003	0.754	Ce/V	mix	-0.025	0.004	0.809
Zr/Si	solar	-0.058	0.016	0.861	Nd/Ti	solar	-0.03	0.006	0.811	Ce/V	solar	-0.034	0.01	0.813
Zr/Ca	poor	-0.006	0.005	0.345	Sr/Eu	poor	-0.022	0.012	0.472	Ce/Al	poor	-0.021	0.006	0.692
Zr/Ca	mix	-0.029	0.004	0.866	Sr/Eu	mix	-0.029	0.01	0.681	Ce/Al	mix	-0.029	0.006	0.824
Zr/Ca	solar	-0.052	0.015	0.847	Sr/Eu	solar	-0.023	0.008	0.7	Ce/Al	solar	-0.035	0.013	0.811
Zr/Ti	poor	-0.008	0.008	0.394	Sr/V	poor	-0.026	0.012	0.423	Nd/Eu	poor	-0.01	0.006	0.409
Zr/Ti	mix	-0.033	0.004	0.876	Sr/V	mix	-0.033	0.005	0.787	Nd/Eu	mix	-0.013	0.007	0.5
Zr/Ti	solar	-0.056	0.018	0.844	Sr/V	solar	-0.041	0.015	0.805	Nd/Eu	solar	-0.012	0.004	0.607
La/Mg	poor	-0.018	0.01	0.591	Sr/Al	poor	-0.026	0.013	0.531	Nd/V	poor	-0.008	0.004	0.451
La/Mg	mix	-0.027	0.006	0.772	Sr/Al	mix	-0.038	0.008	0.785	Nd/V	mix	-0.014	0.004	0.6
La/Mg	solar	-0.03	0.01	0.768	Sr/Al	solar	-0.044	0.017	0.793	Nd/V	solar	-0.035	0.008	0.799
La/Si	poor	-0.013	0.008	0.532	Y/Eu	poor	-0.008	0.007	0.369	Nd/Al	poor	-0.015	0.006	0.504
La/Si	mix	-0.025	0.006	0.782	Y/Eu	mix	-0.019	0.008	0.617	Nd/Al	mix	-0.02	0.005	0.684
La/Si	solar	-0.028	0.012	0.748	Y/Eu	solar	-0.018	0.008	0.474	Nd/Al	solar	-0.039	0.013	0.797